GEORG-AUGUST-UNIVERSITÄT
GÖTTINGEN

Fakultät für
Physik

Master's thesis

Reconstruction of $t\bar{t}Z$ Events Using Kinematic Likelihood Fits at the ATLAS Detector

Kinematische Likelihood-Fits zur Rekonstruktion von $t\bar{t}Z$-Ereignissen am ATLAS-Detektor

prepared by

Knut Zoch

from Wittmund

at the II. Physikalisches Institut

Thesis number:	II.Physik-UniGö-MSc-2016/10
Thesis period:	1 April 2016 until 30 September 2016
First referee:	Prof. Dr. Arnulf Quadt
Second referee:	Prof. Dr. Stan Lai

Abstract

The weak isospin is one of the top quark's properties that has not been measured yet. One way to access this quantity is through the production of a top quark pair in association with a Z boson. The radiation of the Z boson, thus the tZ coupling, directly depends on the weak isospin. The full reconstruction, which is necessary for measurements of the coupling strength and structure, however, comes with difficulties because of the complex final state of three charged leptons, four jets and missing transverse momentum.

Within this thesis, kinematic likelihood fits are introduced as a systematic strategy to reconstruct final states. Different reconstruction methods are discussed and tested to optimise the association of the final-state objects to their origins. The most sophisticated method, a dedicated likelihood, shows the best reconstruction efficiencies with a lepton matching of (88.5 ± 0.6) %. When compared to efficiencies of an existing reconstruction method for $t\bar{t}$ events without an extra vector boson, the $t\bar{t}Z$ reconstruction achieves an overall similar performance. Furthermore, the introduced quantifiers of the reconstruction are shown to be a possible separation variable to discriminate between signal and background.

Zusammenfassung

Eine entscheidende Eigenschaft des Top-Quarks, die bisher experimentell nicht vermessen werden konnte, ist sein schwacher Isospin. Ein Zugang zum Isospin wird beispielsweise durch $t\bar{t}Z$-Ereignisse ermöglicht, bei denen ein Z-Boson von einem Top-Quark abgestrahlt wird. Die Stärke der tZ-Kopplung hängt dabei unmittelbar vom schwachen Isospin ab. Allerdings ist eine Rekonstruktion des $t\bar{t}Z$-Endzustandes aufgrund seiner Komplexität mit drei geladenen Leptonen, vier Jets und fehlendem Transversalimpuls schwierig.

In dieser Masterarbeit werden kinematische Likelihood-Fits als eine systematische Methode vorgestellt, Endzustände zu rekonstruieren. Es werden unterschiedliche Konzepte eingeführt, kinematische Likelihood-Fits für $t\bar{t}Z$-Rekonstruktion zu verwenden. Performance-Vergleiche zeigen, dass eine dedizierte Likelihood dabei die höchsten Effizienzen erreicht: Die Zuordnungseffizienz für Leptonen beträgt (88.5 ± 0.6) %. Verglichen mit einer existierenden Rekonstruktion für $t\bar{t}$-Ereignisse ohne zusätzliches Vektor-Boson weist die entwickelte $t\bar{t}Z$-Rekonstruktion ähnliche Effizienzen auf. Zusätzlich wird gezeigt, dass die Likelihood-Werte, die bei der Rekonstruktion berechnet werden, genutzt werden können, um Signal- und Untergrundereignisse voneinander zu trennen.

Contents

1. Introduction

The Standard Model is a quantum field theory to describe the fundamental particles and their interactions. It was developed in the second half of the 20th century and numerous experiments in the past decades have been consistent with its theoretical predictions with remarkable accuracy. On the contrary, the Standard model cannot be a complete theory of particle physics. There is experimental evidence of several phenomena for which the Standard Model lacks explanations: for instance, if only visible matter is considered, rotations of galaxies show a non-Newtonian behaviour. In order to conserve Newtonian gravity, the observed rotation curves can be explained with a significant amount of *dark matter* [1]. Dark matter, however, is a phenomenon not described by the Standard Model. Other experimental evidence for the incompleteness of the Standard Model was given by the observation of neutrino oscillations [2–4]. These oscillations can only take place if neutrinos are massive particles. This contradicts the Standard Model predictions of massless neutrinos.

Various extensions of the Standard Model have been proposed to account for the aforementioned and other phenomena, with supersymmetry the most popular among them. Within these extensions, the Standard Model is typically embedded in a larger picture, leaving it a valid model within certain restrictions. In the supersymmetric extensions, additional fundamental particles are introduced that form a symmetric counterpart of the already existing Standard Model particles. However, direct evidence for the existence of supersymmetric particles has not been found yet.

Nevertheless, the Standard Model has kept astonishing physicists over the past decades, because an abundance of its predictions have been confirmed experimentally. The last missing piece may have been found recently at the LHC particle accelerator: in 2012, the ATLAS and CMS collaborations discovered a boson [5, 6] which is consistent with the Higgs boson postulated in the 1960s by Higgs [7] and Englert and Brout [8]. The corresponding Higgs mechanism is one of the core aspects of the Standard Model, giving rise to the masses of all fundamental particles. If the discovered boson is indeed confirmed to be the Higgs boson, it will be yet another demonstration of the Standard Model's continued success.

The last major finding in the quark sector of the Standard Model was the discovery of the top quark in 1995 by the CDF and DØ collaborations [9, 10]. It had been the last missing quark predicted by the Standard Model. Since the top quark's discovery, it has been under investigation and some of its properties have not been measured yet. One of these properties, the top quark's weak isospin, remains undetermined despite its paramount importance for validating the Standard-Model likeness of the top quark. A precise measurement of the weak isospin will be a key aspect for confirming that the discovered quark is the anticipated top quark of the Standard Model. If, on the contrary, the isospin is measured to be different from the Standard Model value, it would open doors to physics beyond the established theories.

Particle physics events containing a top-quark pair in association with a Z boson, also simply denoted as $t\bar{t}Z$ events, give access to the tZ coupling. This coupling, in accordance with the Standard Model predictions, depends on the value of the third component of the top quark's isospin. As a consequence, the isospin component can be deduced from precise measurements of the cross section of $t\bar{t}Z$ processes. Although these processes were recently discovered by the CMS collaboration [11], measurements of the cross section have not been accurate enough to allow a determination of the isospin component.

The studies presented within this thesis will focus on the reconstruction of $t\bar{t}Z$ processes. As they come with a complex final state of multiple particles of the same type, their reconstruction is not trivial and systematic methods need to be established. The following studies will introduce kinematic likelihood fits as such a method. Based on the *KLFitter* package [12], alterations and extensions will be presented that allow a reconstruction of the $t\bar{t}Z$ final state with high precision. The reconstruction efficiencies will be evaluated in multiple ways. These include comparisons to established reconstruction methods for the final state of $t\bar{t}$ events without any extra bosons.

Only a fully reconstructed final state will eventually allow precise measurements of the angles between particles. These angular distributions will be an important verification of the Standard Model predictions for the tZ coupling strength and its structure – and therefore of the anticipated value of the weak isospin. The thesis will also address the question as to whether the systematic quantifiers of the reconstruction methods come with separation power between signal and background events. If that is the case, the systematic reconstruction via kinematic likelihood fits can be used as an additional input to multivariate analysis techniques that are utilised in measurements of the $t\bar{t}Z$ cross section.

The next chapter will introduce the theoretical foundation. It includes a general introduction to the physics of the Standard Model, with particular emphasis placed on the physics of the top quark and $t\bar{t}Z$ processes. Chapter 3 introduces the experimental setup of the LHC particle accelerator and the ATLAS experiment, the simulation of which is used to process the Monte-Carlo generated data samples. Chapter 4 explains in detail the *KLFitter* package and the alterations and extensions introduced. It also describes the methods used to evaluate the reconstruction performance. Following that, the results of the studies will be presented in Chapter 5. A summary of the results as well as an outlook can be found in the last chapter.

2. Theoretical Foundation

The basis of modern particle physics is formed by a quantum field theory called the *Standard Model* of elementary particles. Within its limitations, inter alia not incorporating phenomena such as dark matter, the Standard Model describes the particles known today with remarkable accuracy. On the one hand, it consists of twelve fermions, namely six quarks and six leptons, that form all visible and "well-understood" matter of the universe.[1] The fundamental forces, on the other hand, are mediated by the gauge bosons.

In the following section, a brief introduction to the physics of the Standard Model is given. The section covers phenomenological aspects of the three fundamental interactions described within the Standard Model and introduces the elementary particles. Afterwards, Section 2.2 goes into more detail about the top quark, the study of which is of paramount importance for testing the Standard Model predictions. The section will also introduce couplings of the top quark, such as the coupling to the Z boson observed in $t\bar{t}Z$ production. In Section 2.3, processes leading to a $t\bar{t}$ pair in association with a vector boson and measurements of their production cross sections are further discussed.

2.1. The Standard Model of Particle Physics

The Standard Model of particle physics [13–23] includes our present knowledge about matter, its constituents and the forces acting between them. Visible matter is formed by spin-½ particles called fermions. They are separated into quarks and leptons, according to their different coupling behaviour, each consisting of three families. For all twelve fermions there exists an antiparticle with the very same mass, but opposite-sign charges.[2] The forces described by the Standard Model are the weak and electromagnetic interactions (unified to an electroweak theory) as well as the strong interaction. An overview of the particles in the Standard Model is given in Fig. 2.1. Although dominating at large distances, the fourth fundamental force – gravity – has not yet been successfully incorporated and is not described within the Standard Model.

The first generation of quarks is formed by the up quark (u) and the down quark (d),

---

[1] In contrast to the visible matter, a large fraction of the universe is formed by dark matter and dark energy, concepts which are not yet well-understood.

[2] In this context, charge refers to any conserved quantum number that is associated with a generator of a symmetry group. Well-known examples include the electric charge, which is the eigenvalue of the corresponding generator of the $U(1)$ symmetry group.

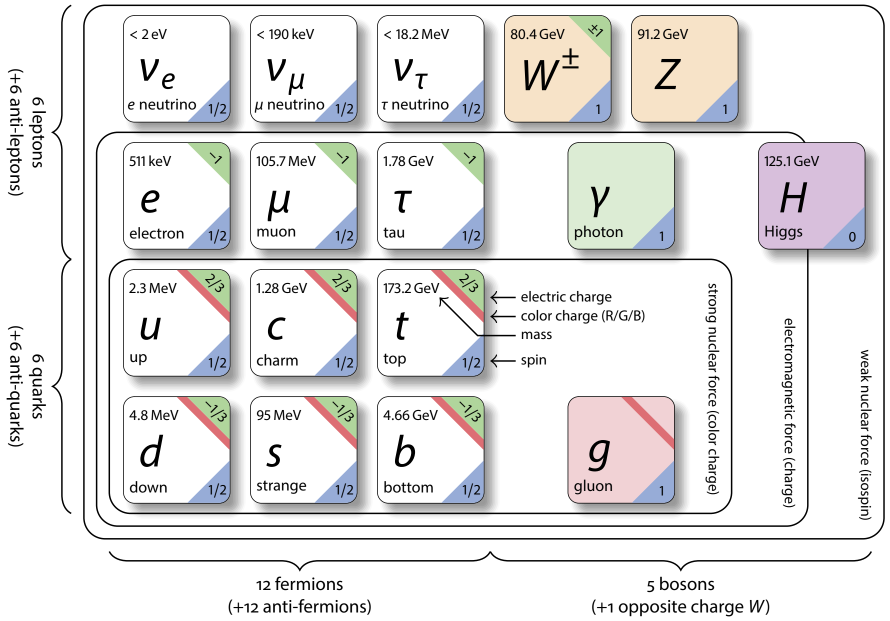

Figure 2.1.: Elementary particles of the Standard Model: twelve fermions forming the luminous matter, the gauge bosons mediating the fundamental forces, and the Higgs boson. Numbers are taken from Ref. [24].

the second one by the charm quark (c) and the strange quark (s), the third one by the top quark (t) and the bottom quark (b). They differ in terms of their quantum numbers such as the third component of the weak isospin[3] I_3 or the electric charge[4] Q. The first quark of each family is called up-type quark and carries $I_3 = +1/2$ and $Q = +2/3$. The other quarks of the respective families are named down-type quarks and carry $I_3 = -1/2$ and $Q = -1/3$. Each quark additionally comes in three different *colour* states. The colour of quarks can be interpreted to be the "charge" quantity of the strong interaction.

The three families of leptons each contain two particles as well: one uncharged and massless neutrino, and one charged, massive lepton. The first family comprises the electron neutrino (ν_e) and the electron (e); the second incorporates the muon neutrino (ν_μ) and the muon (μ). The third consists of the tau neutrino (ν_τ) and the tau (τ). While the neutrinos again carry a weak isospin of $I_3 = +1/2$, the charged leptons carry $I_3 = -1/2$ and $Q = -1$.

The Standard Model itself is a specific quantum field theory with an underlying gauge symmetry $SU(3)_C \times SU(2)_L \times U(1)_Y$. While the fundamental interactions of the particles are described by those gauge fields corresponding to the gauge bosons, the 12 fermions

---

[3] To be precise, only the left-handed fermions carry a weak isospin; the right-handed fermions have $I_3 = 0$. The concept of handedness or *chirality* will be explained in Section 2.1.2.

[4] In the following, the electric charges of particles are denoted in fractions of the elementary charge $e = 1.602 \cdot 10^{-19}$ C. For instance, $Q = 1$ is equivalent to the elementary charge e.

are grouped into doublet and singlet fields according to their weak isospins:

$$\begin{array}{cccc}
Q_L = & \begin{pmatrix} u_L \\ d_L \end{pmatrix} & \begin{pmatrix} c_L \\ s_L \end{pmatrix} & \begin{pmatrix} t_L \\ b_L \end{pmatrix} \\
u_R = & u_R & c_R & t_R \\
d_R = & d_R & s_R & b_R \\
L_L = & \begin{pmatrix} \nu_{eL} \\ e_L \end{pmatrix} & \begin{pmatrix} \nu_{\mu L} \\ \mu_L \end{pmatrix} & \begin{pmatrix} \nu_{\tau L} \\ \tau_L \end{pmatrix} \\
\nu_R = & \nu_{eR} & \nu_{\mu R} & \nu_{\tau R} \\
e_R = & e_R & \mu_R & \tau_R
\end{array} \tag{2.1}$$

The indices L and R denote the left-handed and right-handed chiral states, respectively. The distinction between the chiral states is made because of their differing behaviour in the weak interaction. While the left-handed doublets each contain a fermion with $I_3 = +1/2$ and $I_3 = -1/2$, the right-handed singlets correspond to $I_3 = 0$. The exact differences are explained in more detail in Section 2.1.2 covering the electroweak unification. Prior to that, the following section introduces the strong interaction, described by the theory of *Quantum Chromodynamics*.

2.1.1. Quantum Chromodynamics

Among the 12 fundamental fermions, there are six quarks, each of which carries a colour charge and therefore interacts via the *strong interaction*. The underlying field theory called Quantum Chromodynamics (QCD) is based on an $SU(3)$ gauge group, the generators of which are represented by eight massless spin-1 bosons called gluons (g). They carry both a colour and anti-colour charge. As $SU(3)$ is non-Abelian, the gluons do not only couple to quarks, but also to other gluons. This phenomenon is known as self-interaction and leads to two peculiarities in QCD [19, 20, 25]:

1. *Confinement:* The potential between two quarks does not decrease with their distance, but increases instead, resulting in a constant force. In consequence, quarks are observed only in colour-singlet states in form of hadrons, not as free particles. The confinement makes it preferable to break the colour string between two bound quarks, thus creating another pair of quarks and forming colourless hadronic states again. As a result, quarks created in particle physics experiments, in processes such as $q\bar{q} \to t\bar{t}$, immediately hadronise and form a stream of hadronised particles called *jets*.

2. *Asymptotic Freedom:* For high energies, quarks can be described as asymptotically free particles since the coupling constant of the strong interaction $\alpha_s(q^2)$ decreases as

the energy scale q of the interactions increases. For high energies, perturbation theory can be applied to calculate processes in QCD. Generally, the value of the coupling constant is parameterised according to a known energy scale μ via

$$\alpha_s(q^2) = \frac{\alpha_s(\mu^2)}{1 + \frac{11N_C - 2N_f}{12\pi} \ln\left({}^{q^2}\!/\!{}_{\mu^2}\right)} \tag{2.2}$$

with N_C and N_f being the number of colour states and the number of fermions "available" at the examined energy scale, respectively.

2.1.2. Electroweak Unification

Although the two remaining fundamental forces within the Standard Model – the electromagnetic and the weak interaction – appear to be different concepts with distinct properties, couplings etc., they can be described within a single theory. Because the initial ideas were proposed by Glashow [13], Weinberg [14], and Salam [15], this model of unification is also called the GWS theory.

The theory of the electromagnetic interaction called Quantum Electrodynamics is based on a $U(1)$ gauge symmetry. Its massless gauge boson, the photon (γ), couples to all particles carrying an electric charge Q and is represented by a vector field A_μ. Thus, the coupling term reads

$$j^\mu A_\mu = g_e \overline{\Psi} \gamma^\mu \Psi A_\mu \tag{2.3}$$

where g_e is the electromagnetic coupling constant. The interacting fermions are described by the Dirac spinors $\Psi = \Psi(p)$.

On the other hand, the weak interaction is a more complex theory including both a charged-current and a neutral-current interaction. The first one is mediated by the two charged, massive W gauge bosons. Weak charged currents show a vector-minus-axial-vector behaviour, the structure of which is denoted V–A.[5] The current takes the form

$$j^+_\mu = g_W\ \bar{\nu}\gamma_\mu \frac{1-\gamma^5}{2}\ e = g_W\ \bar{\nu}_L \gamma_\mu e_L \tag{2.4}$$

$$j^+_\mu = g_W\ \bar{u}^i \gamma_\mu \left(\frac{1-\gamma^5}{2}\right) V_{ij}\ d^j = g_W\ \bar{u}^i_L \gamma_\mu V_{ij}\ d^j_L \tag{2.5}$$

with the spinors ν, e, u and d for neutrinos, electrons, up-type and down-type quarks, respectively. The V_{ij} refers to the entry of the CKM matrix for quarks i and j. For the corresponding current j^-_μ, the roles of the spinors ν/e and u/d are reversed within the equations. As shown in the current, the W bosons only couple to left-handed particles

---

[5] A purely vector-like current converts as a vector under Lorentz transformation, whereas an axial vector undergoes an additional sign flip under parity transformation.

and right-handed antiparticles, thus violating parity symmetry. This effect was first observed in the 50s by Wu et al. [26] and led to the conclusion to describe the charged weak interaction as a *chiral* gauge symmetry. The chiral states of particles used in Eq. (2.4), such as e_L and e_R for electrons, are obtained by using the chiral projection operators

$$P_L = \frac{1-\gamma^5}{2}, \qquad P_R = \frac{1+\gamma^5}{2}. \tag{2.6}$$

The two chiral states of a particle are orthogonal. Consequently, the operators satisfy $P_L P_R = 0$ as well as the projection operator relations $P_i^2 = P_i$ and $P_L + P_R = 1$.

To describe the coupling of the charged weak interaction, particles are assigned the weak isospin I. Only if $I \neq 0$, the particle interacts with the W bosons. This is why the fermions are separated into left-handed doublets and right-handed singlets as seen in Eq. (2.1): the W bosons only couple to the doublets, but not to the singlets. Additionally, the third component of the isospin I_3 is always changed by ±1 at the vertex. Thus, the W boson connects the up-type quarks to their respective down-type quarks and the neutrinos to their charged leptons.

However, different experiments, examining the decay of charged kaons K^+, suggested that the charged weak interaction couples *across* the quark families as well.[6] In 1963, Cabibbo [27] proposed a *rotation* of the quark states of the two quark generations known at that time. The implication was that the weak eigenstates do not immediately correspond to the mass eigenstates. Cabibbo's hypothesis was later extended by Kobayashi and Maskawa [28] to a quark mixing matrix of all three families, called CKM matrix:

$$\begin{pmatrix} d' \\ s' \\ b' \end{pmatrix} = \begin{pmatrix} V_{ud} & V_{us} & V_{ub} \\ V_{cd} & V_{cs} & V_{cb} \\ V_{td} & V_{ts} & V_{tb} \end{pmatrix} \begin{pmatrix} d \\ s \\ b \end{pmatrix} \tag{2.7}$$

Here, d', s' and b' denote the weak flavour eigenstates, whereas d, s and b are the mass eigenstates of the down-type quarks. Latest measurements of the magnitudes of the CKM matrix elements yield the following values (see Ref. [24] and references therein):

$$[|V_{CKM,ij}|] = \begin{pmatrix} 0.974\,27 \pm 0.000\,14 & 0.225\,36 \pm 0.000\,61 & 0.003\,55 \pm 0.000\,15 \\ 0.225\,22 \pm 0.000\,61 & 0.973\,43 \pm 0.000\,15 & 0.041\,4 \pm 0.001\,2 \\ 0.008\,86\,^{+0.000\,33}_{-0.000\,32} & 0.040\,5\,^{+0.001\,1}_{-0.001\,2} & 0.999\,14 \pm 0.000\,05 \end{pmatrix} \tag{2.8}$$

The measured values suggest that couplings within the same family are strongly favoured, especially if a quark from the third generation, the top or the bottom quark, is involved. Couplings across generations are often called *suppressed* as they are less likely to occur than couplings within the same generation.

---

[6] The decay of the kaon containing $u\bar{s}$ to $\mu\bar{\nu}_\mu$ could not be explained, otherwise.

In addition to the charged currents, the weak interaction also includes neutral currents mediated by the massive, charge-zero Z boson. The weak neutral current reads

$$J_\mu^{NC} = \overline{\Psi}\,\gamma_\mu\,\frac{c_V^q - c_A^q\gamma^5}{2}\,\Psi \tag{2.9}$$

for the spinor Ψ of a fermion. c_V and c_A are fermion-dependent parameters describing the strength of the vectorial and axial-vectorial couplings.

A unification of the charged and the neutral weak currents seemed impossible since the weak current is a purely V–A-structured coupling, whereas the neutral current is a fermion-dependent mixture of both vectorial and axial-vectorial couplings. However, unification with the electromagnetic interaction leads to a solution: the electroweak currents are described by a purely left-handed theory based on an $SU(2)_L$ group combined with a vector-like $U(1)$ theory. But instead of the electric charge Q, the $U(1)$ group introduces a quantity called *hypercharge* Y for each particle:

$$Q = I_3 + \frac{Y}{2}. \tag{2.10}$$

In consequence, the electroweak interaction can be represented by

$$-ig_W(J^i)^\mu W_\mu^i - i\frac{g'}{2}(j^Y)^\mu B_\mu \tag{2.11}$$

with the three boson fields W_μ^i of the $SU(2)_L$ group and B_μ denoting the boson field of the $U(1)_Y$ group. In electroweak unification, the charged W boson fields correspond to

$$W_\mu^\pm = \sqrt{\frac{1}{2}}\left(W_\mu^1 \mp W_\mu^2\right) \tag{2.12}$$

and the fields of the neutral, massive Z boson and the neutral, massless photon γ (represented by A_μ) are calculated as a superposition of W_μ^3 and B_μ:

$$\begin{pmatrix} A_\mu \\ Z_\mu \end{pmatrix} = \begin{pmatrix} \cos\theta_W & -\sin\theta_W \\ \sin\theta_W & \cos\theta_W \end{pmatrix} \cdot \begin{pmatrix} B_\mu \\ W_\mu^3 \end{pmatrix} \tag{2.13}$$

Their mixing angle θ_W is known as the *weak mixing angle* or *Weinberg* angle. The fermion-dependent parameters c_V and c_A for the neutral weak interaction in Eq. (2.9) are also fixed by the $SU(2)_L \times U(1)_Y$ theory. They can be calculated via the electric charge Q and the third component of the weak isospin I_3 of the respective fermion f:

$$c_V^f = I_3^f - 2Q_f\sin^2\theta_W \tag{2.14}$$

$$c_A^f = I_3^f \tag{2.15}$$

The GWS theory also establishes a relationship between the two coupling constants g_e and g_W and between the masses of the three massive bosons $W^\pm$ and Z:

$$g_W = \frac{g_e}{\sin\theta_W} \qquad M_Z^2 = \frac{M_W^2}{\cos^2\theta_W} \tag{2.16}$$

Acquisition of the boson masses within the electroweak theory takes place by demanding local gauge invariance and spontaneous symmetry breaking. The mechanism is known as the Higgs or Brout-Englert-Higgs mechanism honouring the three physicists who proposed the mechanism [7, 8]. Direct mass terms within the Lagrangian of the Standard Model would violate the demanded gauge invariance. The spontaneous symmetry breaking of the Higgs mechanism explains the acquisition of masses for the fermions as well: *Yukawa* terms coupling Higgs and fermions are introduced to the Lagrangian. As it is one of the heaviest quarks, the Yukawa coupling for the top quark is by far the strongest and, consequently, its role within the Standard Model is of particular importance. The next section will give an overview over the physics of the top quark.

2.2. Top Quark Physics

Seeking an explanation for the charge-parity violation observed in the 60s by Cronin et al. [29], in 1973 Kobayashi and Maskawa proposed to expand the quark sector by a third generation – thereby postulating another up- and down-type quark [28]. Although they were eventually discovered as the bottom and the top quark, the latter one only in 1995, there had been an accumulation of evidence pointing towards their existence in the intermediate period.

With the discovery of the tau lepton in 1975 [30], a third generation of leptons was established, being a strong indicator that a third generation of quarks exists as well. No more than two years later, the bottom quark was discovered [31]. Not only did it show the expectation of a third quark generation to be true, but it also raised the question of the existence of another third-generation quark as the bottom quark was presumed to come in an $SU(2)$ doublet as well. There are two reasons to suspect so:

Firstly, there is the GIM mechanism [16] proposed in 1970 by Glashow et al. to naturally suppress flavour-changing neutral currents (FCNC) and to explain the different behaviour of processes involving strangeness changes.[7] Postulating the existence of the charm quark four years before its discovery, the mechanism was originally introduced involving two quark doublets, but works just as well with three $SU(2)$ quark doublets. Now assuming the bottom quark to be an $SU(2)$ singlet as suggested in several models without any top quark [34–37], the natural suppression of FCNC by the GIM mechanism would be

---

[7] Strangeness is a concept introduced by Gell-Mann and Nishijima [32, 33] to explain the relatively slow decay of particles comprising the strange quark, such as kaons.

spoiled and FCNC would be observed in the decay of the bottom quark. Measurements, for example by the UA1 collaboration, set limits on the corresponding branching fractions and excluded the $SU(2)$ singlet hypothesis [38].

Secondly, it is desirable to incorporate the weak interactions in a *renormalisable* theory, such as the electroweak unification of the Standard Model [13–15, 22]. While retaining the model free of anomalies is not of vital importance to *obtain* renormalisability, it is a necessary precondition to apply the general proof of it. It can be shown that an anomaly-free theory is only achieved if the number of quarks equals the number of leptons (assuming every quark exists in three colour states). Apart from the three discovered charged leptons, the number of (light) neutrinos had been determined to be $N_\nu = 3$ from Z mass pole precision measurements at LEP [39]. Therefore, a renormalisable theory of weak interactions strongly suggested the existence of the top quark as well to match the number of leptons.

After many indirect searches for the top quark and constraints on its mass, it was eventually discovered in 1995 by the TEVATRON collaborations CDF and DØ [9, 10]. Today, the LHC is the only operating collider that is able to produce top quarks since the TEVATRON's shutdown in 2011.

Within the Standard Model, the top quark is of particular interest because of its uniquely high mass. A 2016 combination of measurements from the TEVATRON collaborations yielded a top quark mass of [40]:

$$m_t = 174.30 \pm 0.35(\text{stat}) \pm 0.54(\text{syst})\,\text{GeV} \tag{2.17}$$

corresponding to a total uncertainty of 0.65 GeV which is approximately 0.37%. The mass translates to a Yukawa coupling factor of the top quark close to unity and leads to the belief that the top quark – being more than 30 times heavier than the second heaviest quark, the bottom quark – potentially plays a special role in electroweak symmetry breaking or even opens windows to new physics beyond the Standard Model.

The top quark's large mass also results in a remarkably short lifetime τ_t. Jeżabek and Kühn calculated its decay width corresponding to $\Gamma_t = \hbar/\tau_t$ at next-to-leading order (NLO) to be [41]

$$\Gamma_t \overset{(NLO)}{=} \frac{G_F m_t^3}{8\pi\sqrt{2}} \left(1 - \frac{M_W^2}{m_t^2}\right)^2 \left(1 + 2\frac{M_W^2}{m_t^2}\right) \left[1 - \frac{2\alpha_s}{3\pi}\left(\frac{2\pi^2}{3} - \frac{5}{2}\right)\right] \tag{2.18}$$

which yields an expected decay width of about $\Gamma_t \approx 1.3\,\text{GeV}$. Hence, the resulting lifetime of $\tau_t \approx 0.5 \cdot 10^{-24}\,\text{s}$ is shorter than the typical hadronisation timescale by about two orders of magnitude [42]. As a consequence, top quarks generally decay before hadronisation and before bound states are formed. That being the case, studying the decay of top quarks is of special interest because the properties of the "bare" quark are transferred directly to its decay products.

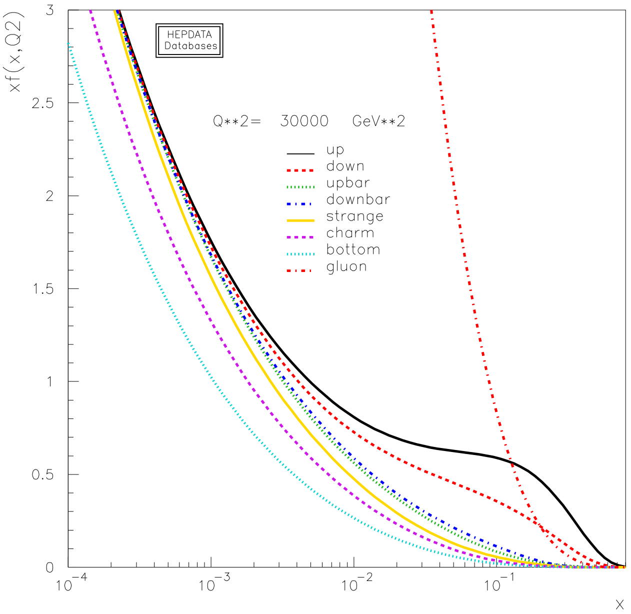

Figure 2.2.: Momentum fractions of quarks and gluons in the proton for the NNPDF2.3 PDF set [43] at a factorisation scale of $\mu_f^2 = Q^2 = 30\,000\,\mathrm{GeV}^2 \approx m_t^2$. This figure was created with Ref. [44].

2.2.1. Top Quark Pair Production

Since the top quark's discovery, it has only been produced at the TEVATRON accelerator at FERMILAB and the LHC at CERN. Because both accelerators are hadron colliders, pair production ($t\bar{t}$) is the predominant process to produce top quarks. The hard scattering process between two hadrons is in fact an interaction between their constituents called partons, i.e. their valence quarks, sea quarks and gluons. The partons each carry a certain momentum fraction x of their respective hadron's momentum. The probability of observing a particular parton with momentum fraction x at a fixed *factorisation scale* μ_f is described by the *parton distribution function*, usually shortened to PDF. For a factorisation scale of $\mu_f^2 = 30\,000\,\mathrm{GeV}^2$ which approximately corresponds to the mass scale of the top quark, the parton distribution functions $f_i(x_i, \mu_f^2)$ of quarks and gluons are plotted in Fig. 2.2 using the NNPDF2.3 PDF set [43].

The inclusive cross section of top quark pair production at a hadron collider like the LHC (where $t\bar{t}$ pairs are produced via proton-proton collisions) can be calculated using the factorisation theorem. The cross section can be expressed as a convolution of PDFs and the partonic cross section $\hat{\sigma}$ [45, 46]:

$$\sigma_{t\bar{t}}(\sqrt{s}, m_t) = \sum_{i,j=q,\bar{q},g} \int dx_i \, dx_j \, f_i(x_i, \mu_f^2) \, f_j(x_j, \mu_f^2) \qquad (2.19)$$

$$\times \, \hat{\sigma}_{ij \to t\bar{t}}(\hat{s}, x_i, x_j, m_t, \mu_f, \alpha(\mu_f^2))$$

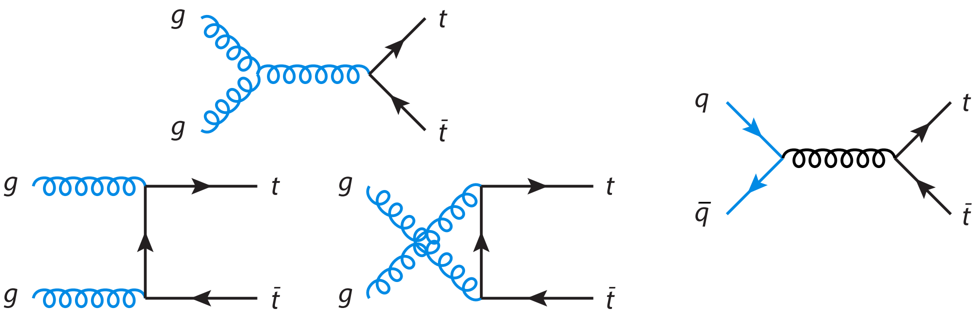

(a) (b)

Figure 2.3.: Leading-order Feynman diagrams for $t\bar{t}$ production at hadron colliders. The production is possible via either a) gluon-gluon fusion or b) $q\bar{q}$ annihilation.

Here, $f_i(x_i, \mu_f^2)$ denotes the PDF of parton i as a function of its momentum fraction x_i. μ_f represents the chosen factorisation scale and $\hat{s}$ stands for the effective squared centre-of-mass energy of the parton-parton interaction process, thus satisfying $\hat{s} = x_i x_j s$ with the centre-of-mass energy s of the proton-proton process. In order to produce a $t\bar{t}$ pair, the parton-parton interaction has to satisfy $\hat{s} \geq 4m_t^2$.

At hadron colliders, $t\bar{t}$ production can take place via either gluon-gluon fusion or $q\bar{q}$ annihilation. The corresponding Feynman diagrams can be seen in Fig. 2.3. The TEVATRON collided protons and antiprotons at a maximum centre-of-mass energy of $\sqrt{s} = 1.96\,\text{GeV}$ during Run II. Since momentum fractions at the order of $x \sim 0.2$ were needed to produce $t\bar{t}$ pairs, the predominant production process was $q\bar{q}$ annihilation with a probability of about 85%, whereas $t\bar{t}$ production at the LHC is vastly dominated by gluon-gluon fusion processes. At centre-of-mass energies of 13–14 TeV in Run II, $t\bar{t}$ pairs are produced via gluon-gluon fusion in about 90% of the cases. Moreover, due to these high energies, a large fraction of top quark pairs is expected to be produced well above the mass threshold – also entering the *boosted* regime where the invariant masses $m_{t\bar{t}}$ are very high and the decays can no longer be fully resolved due to overlapping jets in the detector.

Assuming $m_t = 173.2\,\text{GeV}$, the predicted cross section for $t\bar{t}$ production at the LHC during Run II with a centre-of-mass energy of $\sqrt{s} = 13\,\text{TeV}$ is

$$\sigma_{pp\to t\bar{t}} = 816.0\ ^{+19.4}_{-28.6}(\text{scale}) \pm 34.4(\text{PDF}+\alpha_s)\ ^{+22.7}_{-22.0}(m_t)\ \text{pb} \tag{2.20}$$

as calculated with the Top++2.0 program to next-to-next-to-leading order in perturbative QCD, including soft-gluon resummation to next-to-next-to-leading-logarithmic order (see Ref. [47] and references therein).[8]

---

[8] The first uncertainty comes from the independent variation of the factorisation and renormalisation scales, μ_F and μ_R, while the second one is associated to variations in the PDF and α_s, following the PDF4LHC prescription with the MSTW2008 68% C.L. NNLO, CT10 NNLO and NNPDF2.3 5f FFN PDF

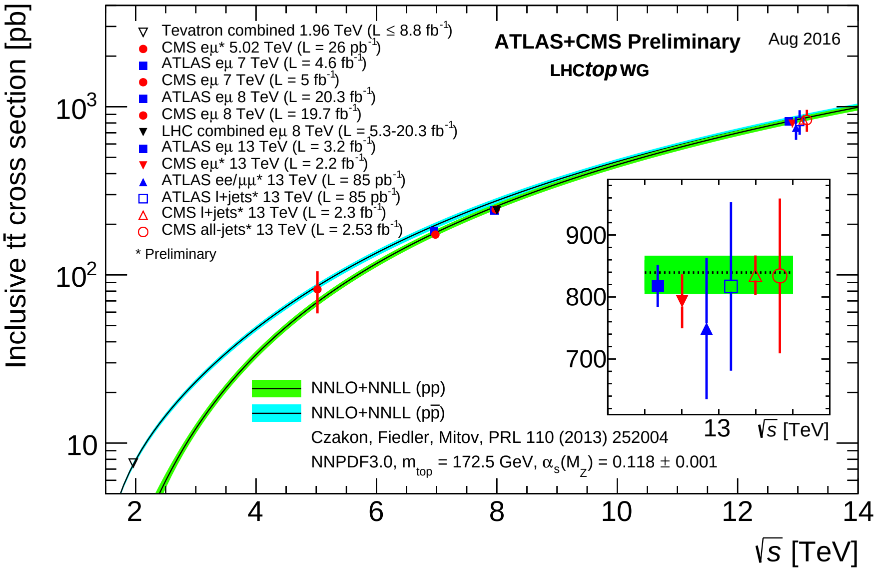

Figure 2.4.: Measurements and theory predictions for the inclusive cross section for $t\bar{t}$ production at pp and $p\bar{p}$ colliders. Figure taken from Ref. [52].

An overview of measurements of the $t\bar{t}$ production cross section performed by the TEVATRON collaborations as well as ATLAS and CMS can be found in Fig. 2.4, also showing the theory predictions for pp and $p\bar{p}$ colliders for comparison. The most recent measurement of $\sigma_{t\bar{t}}$ at 13 TeV published by ATLAS using data corresponding to an integrated luminosity of 3.2 fb^{-1} yielded [51]

$$\sigma_{t\bar{t}} = 818 \pm 8(\mathrm{stat}) \pm 27(\mathrm{syst}) \pm 19(\mathrm{lumi}) \pm 12(\mathrm{beam})\ \mathrm{pb}, \tag{2.21}$$

being in good agreement with the theory prediction stated in Eq. (2.20).[9]

2.2.2. Single Top Quark Production

Apart from $t\bar{t}$ pair production, top quarks can also be produced as single particles. At leading order, there are three types of processes resulting in a single top quark in the final state: t-channel production via W exchange, s-channel production with a W boson decaying to a top quark and a down-type quark (usually b) and Wt production. The latter one is also known as *associated* production since the final state contains both a W boson and a top quark. Feynman diagrams of all three production types can be found in Fig. 2.5.

Since single top quark production has large irreducible backgrounds and production at the TEVATRON long lacked statistics to overcome them, electroweak single top quarks

---

sets (see Ref. [48] and references therein, and Ref. [43, 49, 50]).

[9] The measurement was performed in the dilepton channel with an opposite-sign e-μ pair.

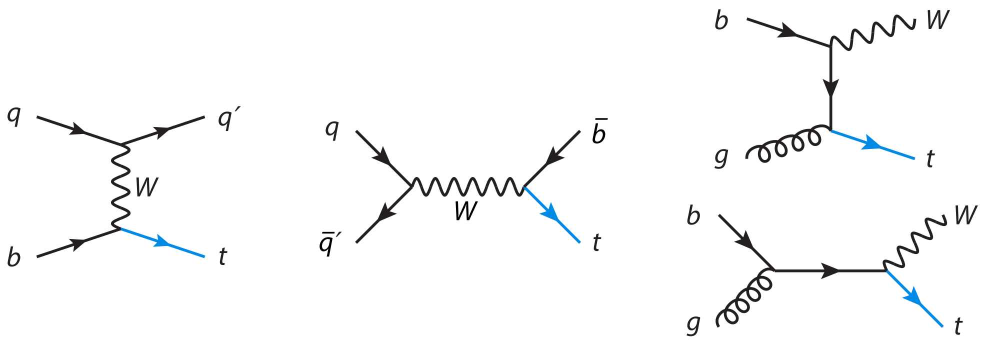

(a) (b) (c)

Figure 2.5.: Leading-order Feynman diagrams for single top production at hadron colliders. Top quarks originate from a) t-channel production, b) s-channel production or c) associated production with a *Wt* final state.

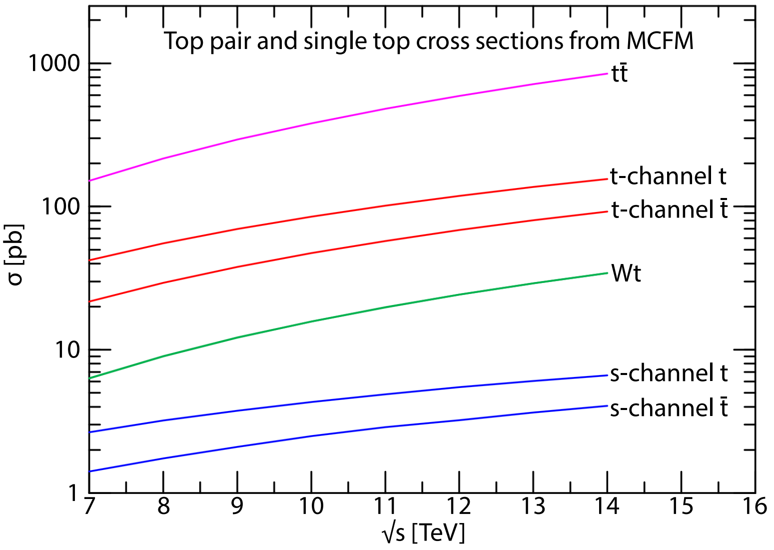

Figure 2.6.: Cross section for the different single top production processes in comparison with the $t\bar{t}$ cross section. Figure created with Ref. [55].

were only observed in 2009 by the CDF and DØ collaborations [53, 54]. Theory predictions for the three single top production modes as a function of the centre-of-mass energy can be seen in Fig. 2.6. For comparison, the figure also shows the cross section of $t\bar{t}$ production.

2.2.3. The Decay of the Top Quark

Due to its broad decay width, the top quark decays very quickly mediated by the weak interaction. In the Standard Model, the only possible decay is to a W boson and a down-type quark – the most likely being the bottom quark due to the large CKM matrix element V_{tb} as seen in Eq. (2.8). Decays to the strange and the down quarks are strongly suppressed.

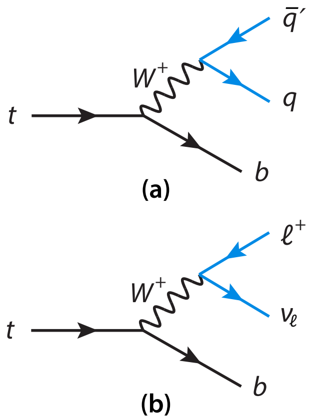

Figure 2.7.: Diagrams of a) the hadronic and b) the leptonic decay of the top quark.

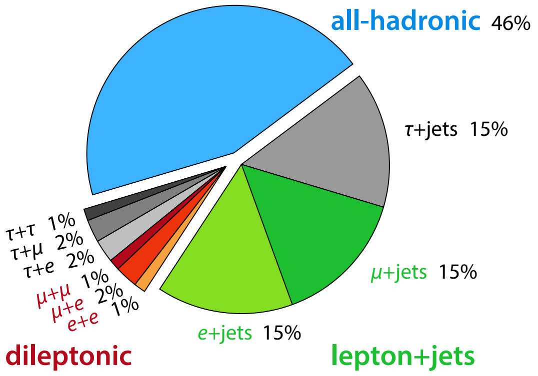

Figure 2.8.: Decay channels of a top quark pair and their branching fractions.

Either way, the down-type quark immediately hadronises while the W boson further decays to lighter particles.

The decay of the W is either possible to quarks or leptons. The branching fractions can roughly be estimated by the following approximation: Neglecting cross-family coupling of the W, there are two quark families and three lepton families the W can decay to at leading order.[10] Including the colour factor, this leads to a total of six possible quark decays. Therefore, the ratio of decays to quarks and decays to leptons is roughly $2:1$. The same ratio applies for the hadronic and leptonic decays of the top quark. Feynman diagrams of both types can be seen in Fig. 2.7.

For a top quark pair $t\bar{t}$, there are three possible decay channels: the *dileptonic*, the *lepton+jets* and the *all-hadronic* channel. While in the first case both top quarks decay to leptons, in the lepton+jets channel one top quark goes to leptons and the other to hadrons. In the all-hadronic case, both top quarks decay hadronically. A pie chart of all possible decay channels including their branching fractions is shown in Fig. 2.8.

Whereas the all-hadronic channel comes with an immense contribution of background processes, such as multijet production, the kinematics of the dileptonic channel cannot be resolved entirely due to the two missing neutrinos in the final state. Consequently, difficulties accompany measurements in both channels: in the former case, separating signal from background; in the latter, reconstructing the $t\bar{t}$ final state. The lepton+jets channel, on the other hand, is used for measurements frequently. Requiring an isolated lepton from one of the top quark decays suppresses the multijet background that dominates the all-hadronic channel. The kinematics are still possible to be resolved since the events contain only one undetected neutrino.

---

[10] The third quark generation is not accessible due to energy-momentum conservation.

2.2.4. Couplings of the Top Quark

In addition to its weak decay via W bosons, the top quark is subject to all other fundamental forces of the Standard Model. The couplings to bosons can be used to examine the properties of the top quark. Although the top quark was discovered more than twenty years ago, many of its properties are still under investigation and their precise measurement is crucial to complete the picture of the top quark anticipated by the Standard Model. Moreover, comparing measurements of the top quark's properties with predictions is pivotal to test the consistency of the Standard Model in general.

Two ways to access the coupling of the top quark to W bosons have been described already: the top quark's decay and single top production. While the Standard Model predicts $|V_{tb}| \approx 1$ in the CKM matrix, the matrix element would be significantly smaller if a fourth generation of quarks existed. Measurements of $|V_{tb}|$ and in consequence of the Wtb coupling can be extracted from the ratio of the two processes $t \to Wb$ and $t \to Wq$. Within single top production, the coupling strength of the Wtb vertex can be directly extracted from cross section measurements.

Another method to study the Wtb vertex structure is the helicity of the W boson in top quark decays. Since the top quark decays before its hadronisation, its spin information is transferred to its decay products. Measuring the fractions of the three possible W boson polarisation states (left-handed, right-handed and longitudinal) by investigating the angular distributions of the W boson decay products tests the coupling behaviour predicted by the Standard Model.

The top quark's coupling to the Higgs boson, the Yukawa coupling term, is another key aspect in verifying predictions by the Standard Model. Indirect constraints on the coupling can be set from the production rate of Higgs bosons at hadron colliders: the production of Higgs bosons via gluon-gluon fusion is only possible via loop diagrams. Since the Yukawa coupling of the top quark is by far the strongest, top quarks dominate those loops and consequently the production rate depends on the tH coupling. Direct measurements of the coupling can be obtained from processes with tH and $t\bar{t}H$ final states. Neither the ATLAS nor the CMS collaboration has claimed an observation of $t\bar{t}H$ signal so far, but at present it is one of the most extensively studied processes.

The coupling of top quarks to photons is best measured in the *associated* production of photons, generally described as $t\bar{t}\gamma$ processes. It has to be taken into account that photons can also be radiated at other stages of the pair production, for instance by one of the decay products after the top quark's decay.

Similarly, a top quark pair can be produced with an associated Z boson in $t\bar{t}Z$ processes and gives direct access to the coupling of the top quark to the Z boson. Generally, a measurement of the coupling would also be possible if the top quark pair were produced via a virtual Z boson in processes like $q\bar{q} \to Z^* \to t\bar{t}$, but at high centre-of-mass energies, production via QCD as described in Section 2.2.1 dominates overwhelmingly. The next

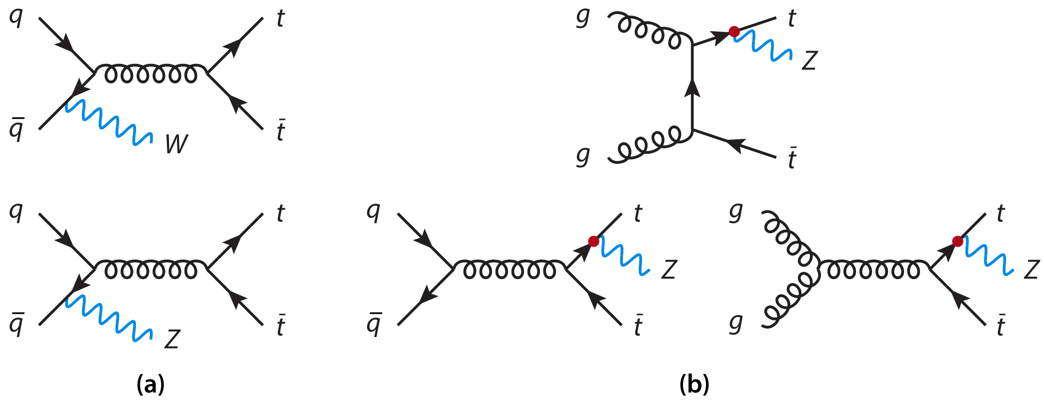

Figure 2.9.: Leading-order Feynman diagrams for $t\bar{t}$ production with an associated vector boson: a) as initial state radiation, b) as final state radiation.

section will discuss the processes with a $t\bar{t}Z$ final state, also including measurements of their cross sections by ATLAS and CMS.

2.3. $t\bar{t}Z$ Production

Measuring the couplings of the top quark to the gauge bosons, as introduced in the previous section, has two primary outcomes: an accurately measured coupling strength can either lead to a confirmation of the top quark's properties, as anticipated by the Standard Model, or establish new physics beyond. Investigations of processes involving the coupling between the top quark and the Z boson allow tests of the weak neutral current introduced in Eq. (2.9). The strength and structure of the coupling between the top quark and the Z boson, parameterised by the fermion-dependent constants c_V and c_A, depends directly on the value of the top quark's weak isospin I_3. It therefore reads

$$\mathcal{L} = \frac{g_Z}{2}\left[\bar{u}(p_t)\,\gamma^\mu(c_V - \gamma_5 c_A)v(p_{\bar{t}})\right]\,Z_\mu \qquad (2.22)$$

where $c_V = I_3 - 2Q_t \sin^2\theta_W$ and $c_A = I_3$, as seen in Eq. (2.14). Consequently, with an electric charge $Q = +2/3$ that has been confirmed experimentally and with a precise value for the weak mixing angle, measured by the LEP collaborations [56], the isospin component I_3 can be determined. Although there are strong indications that the top quark carries $I_3 = +1/2$ and is the isospin doublet partner of the bottom quark, only a direct measurement of its isospin can confirm the hypothesis.

One process, in which the tZ coupling as seen in Eq. (2.22) occurs directly, is the production of a top quark pair with an associated Z boson. In Fig. 2.9, Feynman diagrams of the leading-order processes for both $t\bar{t}Z$ and $t\bar{t}W$ production can be seen. The Z boson can be radiated as either *initial state* or *final state* radiation. The W boson can be radiated

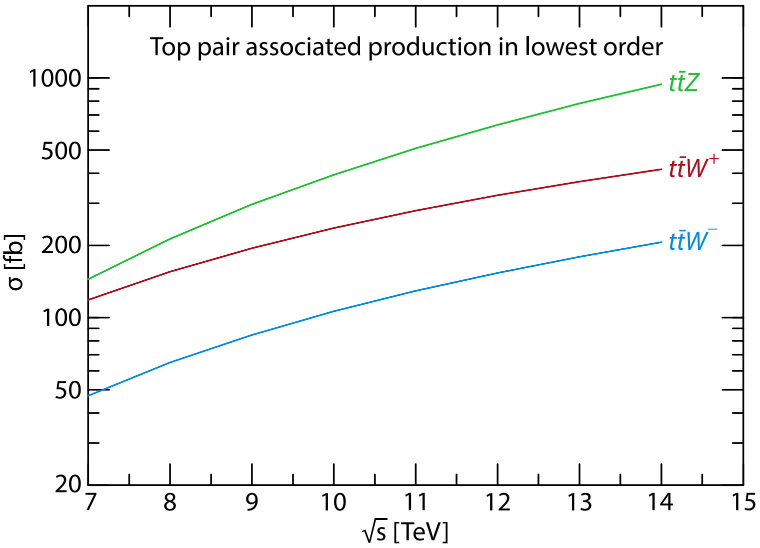

Figure 2.10.: Cross section predictions for $t\bar{t}Z$ and $t\bar{t}W$ production at proton-proton colliders. As the energy increases, $t\bar{t}Z$ production becomes more dominant compared to $t\bar{t}W$. Figure created with Ref. [55].

from the initial state only. While the final states of both ISR and FSR look alike for $t\bar{t}Z$ production, only the latter is of interest for the tZ coupling. The corresponding vertices are marked in red.

Fig. 2.10 shows predictions of the cross sections for both $t\bar{t}Z$ and $t\bar{t}W$ processes. Since the production of a W^+ boson is more likely to occur at proton-proton colliders, $t\bar{t}W$ events are separated into events containing W^+ and W^- bosons. The diagram shows that $t\bar{t}Z$ processes become more dominant compared to $t\bar{t}W$ processes as the energy increases which is caused by their production mechanisms: the diagram in Fig. 2.9 reveals that the radiation of a W boson is only possible in quark-antiquark initial state. As the energy increases, however, $t\bar{t}$ production via gluon-gluon fusion becomes more dominant, described in detail in Section 2.2.1. This causes the fraction of $t\bar{t}W$ processes to decrease compared to $t\bar{t}Z$.

The cross section of $t\bar{t}Z$ at 13 TeV at the LHC is expected to be about three orders of magnitude below that of top pair production. A calculation of the MADGRAPH5_aMC collaboration at next-to-leading order yielded [57]:

$$\sigma_{t\bar{t}Z} = 0.76\ ^{+9.7\%}_{-11.1\%}(\text{scale})\ ^{+1.9\%}_{-2.2\%}(\text{PDF})\ \text{pb} \tag{2.23}$$

On the experimental side, measurements of $t\bar{t}Z$ production have been performed at the LHC by both the ATLAS and CMS collaborations. Measurements at 7 TeV and 8 TeV showed good agreement with the corresponding theory predictions [11, 58–60]. For

13 TeV, the two LHC collaborations measured [61, 62]

$$\text{ATLAS:} \quad \sigma_{t\bar{t}Z} = 0.92 \pm 0.29(\text{stat.}) \pm 0.10(\text{syst.})\ \text{pb} \tag{2.24}$$

$$\text{CMS:} \quad \sigma_{t\bar{t}Z} = 0.70\ {}^{+0.16}_{-0.15}\ (\text{stat.})\ {}^{+0.14}_{-0.12}\ (\text{syst.})\ \text{pb} \tag{2.25}$$

which also agrees with the prediction in Eq. (2.23) within uncertainties.

3. Experimental Particle Physics at the LHC

With very few exceptions, the particles of the SM are not observed in nature as free particles. In order to examine them, they have to be produced artificially at high-energy physics experiments. Exploiting the energy-mass equivalence, particles are accelerated to velocities close to the speed of light and then collided. Mediated by the fundamental interactions of the Standard Model, new particles arise from the energy released during the collision processes. For economical reasons, many particle accelerators are built in a circular shape where the particles reach the desired energy after many revolutions. Particle beams traversing in opposite directions are injected into two separated beam pipes. Although the term *beam* is commonly used, particles are not accelerated as a continuous stream, but as *bunches* of particles instead.

The particles created at the circular accelerator LHC are observed with the state-of-the-art detectors ATLAS and CMS to reconstruct precisely the final-state products of these collisions. One major difficulty in the process of the reconstruction is the fact that the artificially produced particles decay very quickly – many of them already before detection, generating a plethora of lighter particles. Hence, particle detectors need to capture many particles accurately at the same time to enable precise reconstruction. The following sections describe the operation of the LHC and one of the LHC detectors, the ATLAS experiment.

3.1. The Large Hadron Collider (LHC)

The Large Hadron Collider (LHC), the world's most powerful particle accelerator, was operated with centre-of-mass energies of 7 and 8 TeV during Run I (2010–2012). During the current Run II, data is taken at 13 TeV with a potential increase to 14 TeV. The LHC accelerator is operated by the European Organization for Nuclear Research, established in 1954, and usually abbreviated to CERN (French: *Conseil Européen pour la Recherche Nucléaire*). As of September 2016, CERN holds 22 member states. Just like the CERN headquarters, the LHC is located close to Geneva at the Franco-Swiss border.

The LHC is a circular accelerator with a circumference of 26.7 km. Due to the large diameter of the ring structure and to minimise external influences, such as cosmic radi-

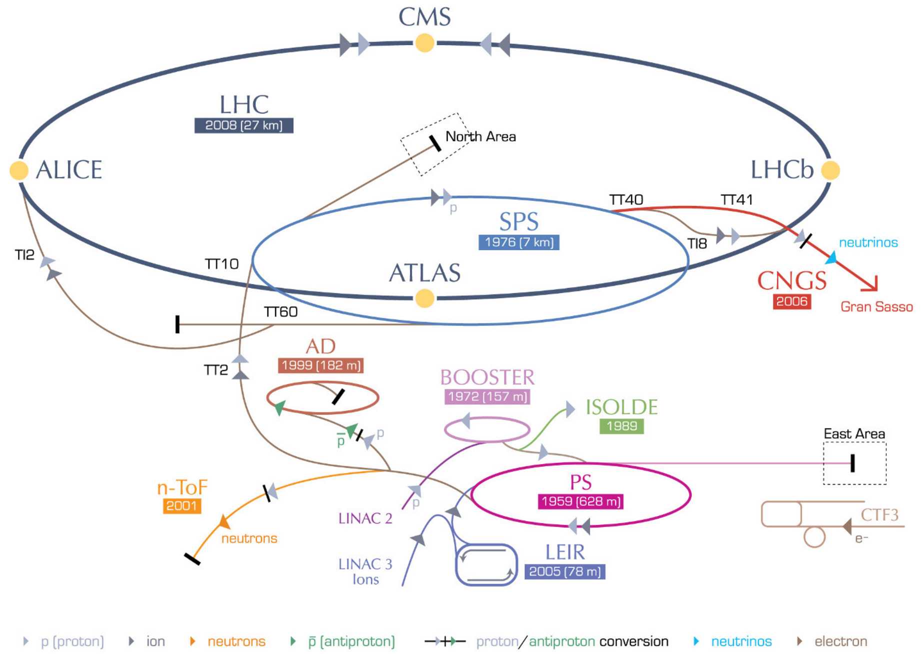

Figure 3.1.: The CERN accelerator complex with all pre-accelerator stages of the LHC. ©CERN

ation, it is located in a tunnel about 100 m below ground. The two adjacent beam pipes intersect at four different collision points. Acceleration of the particles is provided by a total of 16 radio-frequency cavities, operating at a maximum voltage of 2 MV each, resulting in 16 MV in total per beam. More than 1 600 dipole and quadrupole magnets are installed to bend the beams on their circular path and to focus them. In order to operate those magnets made of superconductive material, an operating temperature below 2 K is provided by a liquid-helium cooling system. Additionally, the beam pipes are evacuated to prevent scattering of the accelerated particles with gas molecules.

The main experimental focus of the LHC is on high-energy proton-proton collisions although other types of experiments, for instance collisions involving heavy ions, are conducted as well. The acceleration takes place in multiple pre-accelerator stages; when injected to the main LHC ring, the particles carry energies of 450 GeV already. A diagram showing the different accelerator facilities connected with the LHC is shown in Fig. 3.1.

Data taking at the LHC started in 2010 with about 3.5 TeV energy per beam, thus, with a total centre-of-mass energy of $\sqrt{s} = 7\,\text{TeV}$.[1] For 2012, the system was upgraded to 8 TeV. From February 2013, the operation was interrupted for a major upgrade until early 2015. Since then, the LHC has been running at a centre-of-mass energy of 13 TeV – that will eventually be increased to 14 TeV.

Whereas the intensity of the particle beams of a collider is usually described with the

---

[1] That energy corresponds to a Lorentz factor γ close to 10 000 and leads to a revolution frequency of the proton bunches of approximately 11 kHz.

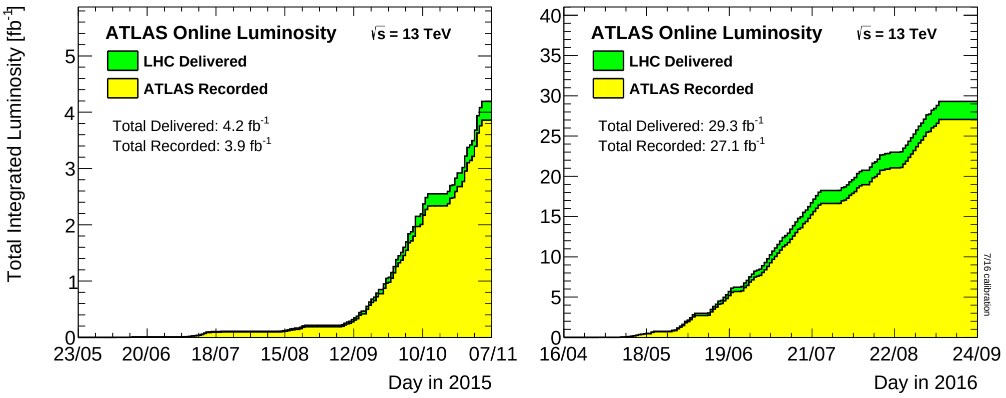

(a) **(b)**

Figure 3.2.: Integrated luminosity of the LHC in a) 2015 and b) 2016 as recorded by the ATLAS detector [63].

instantaneous luminosity $\mathcal{L}$, the *integrated* luminosity $\int \mathcal{L}dt$ is a measure for the amount of data collected in a certain period of time.[2] During Run I of the LHC, the ATLAS experiment collected data corresponding to 5.08 fb^{-1} and 21.3 fb^{-1} at energies of 7 and 8 TeV, respectively. In figure Fig. 3.2, the total integrated luminosity collected by ATLAS in 2015 and 2016 is displayed. For comparison, the total amount of data collected by the CDF and DØ collaborations during Run II of the TEVATRON collider from 2001 to 2011 corresponds to about 10 fb^{-1} of integrated luminosity.

In total, the LHC accelerator accommodates seven experiments analysing different types of physics phenomena. While the two main detectors ATLAS and CMS serve multiple purposes, the experiments ALICE and LHCb are specialised on heavy ions and b-quark physics, respectively. The three remaining detectors TOTEM, MoEDAL and LHCf cover specific areas, for example LHCf works on issues in the field of astroparticle physics.

3.2. The ATLAS Detector

In terms of dimensions, the ATLAS detector is the largest of the LHC experiments. It is about 44 m long, 25 m in diameter, and weighs approximately 7 000 tons. The detector is operated by the ATLAS collaboration involving more than 3 000 scientists. The following paragraphs summarise the main detector components and are based on the technical design report of the ATLAS detector [64].

Figure 3.3 shows the concentric construction of the detector: the innermost component, called the *inner detector*, comprises the pixel detector, the semiconductor tracker and the

---

[2] The luminosity sets the production rate $\dot{N}$ and the cross section σ of a process in relation via $\mathcal{L} = \dot{N}/(\sigma A\epsilon)$ where A and ϵ are the acceptance and the detecting efficiency of the used detector, respectively.

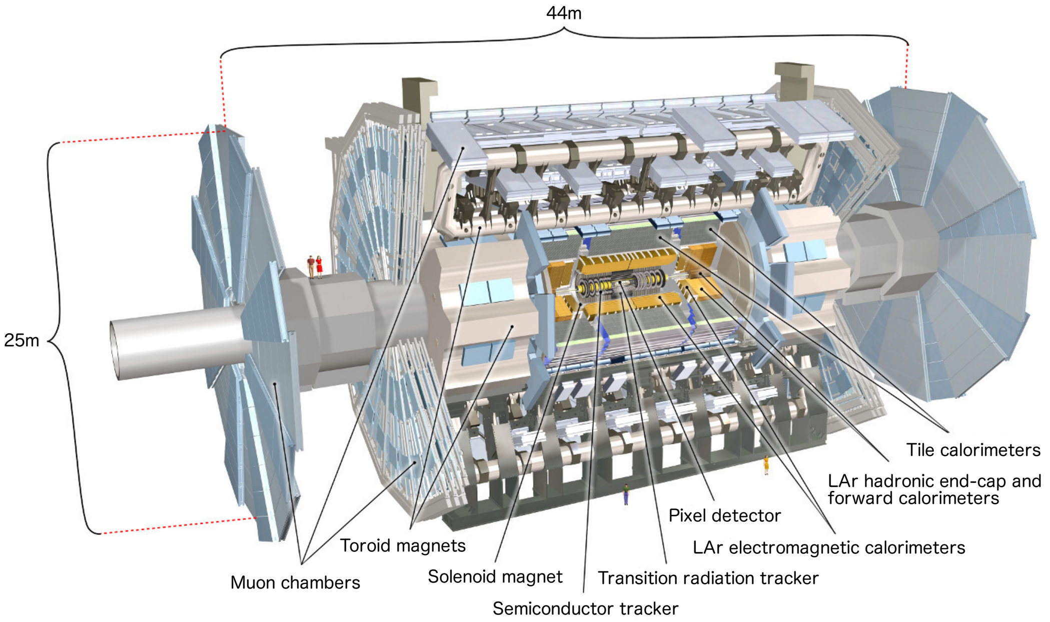

Figure 3.3.: Overview of the structure of the ATLAS detector. ©CERN

transition radiation tracker. It is constructed to be as close to the beam axis as possible: its innermost component, the *Insertable B-Layer*, added during the shutdown in 2013, has an inner radius of only 3.3 cm. The inner detector in total extends up to a radius of 115 cm around the beam pipe. All parts of the inner detector are designed to measure precisely spatial information, such as the transverse momenta and the directions of the emerging particles. The innermost layer of the inner detector is the *pixel detector*, consisting of a total of four pixel layers including the recently added Insertable B-Layer and two end-caps. The layers and end-caps contain a large number of semiconductor pixels which are triggered when charged particles pass through. Because of the proximity to the interaction point, the material has to be radiation-hard. The middle component of the inner detector, the *semiconductor tracker*, consists of silicon strips covering larger areas than the pixels. Although the granularity of the tracker is much lower than that of the pixel detector, the combination of both gives precise tracking information. The *transition radiation tracker*, the outermost layer of the inner detector, is based on a detection method similar to straw detectors: chambers, using ionisation detection, provide additional tracking information and identification criteria to separate signals of different particle types.

Around the inner detector, a solenoid magnet system with $B = 2\,\mathrm{T}$ is installed to force the traversing charged particles on a curved trajectory. Not only does the direction of the curvature serve as an indicator for the particles' electric charges, but also the degree of curvature permits a calculation of the momenta of the particles. Uncharged particles can be distinguished as they do not produce any tracks at all.

Outside the solenoid magnets, two different types of calorimeters are installed: the *electromagnetic* and the *hadronic calorimeters*, both serving the purpose of measuring the energy of the particles. The ATLAS calorimeters are *sampling* calorimeters; they comprise two different layers: a high-density metal to induce energy losses and a layer where the deposited energy is determined.

The electromagnetic calorimeter is made of lead and liquid argon (LAr), the hadronic calorimeter consists of plastic scintillator plates embedded in an iron absorber. Whereas the electromagnetic calorimeter is intended to detect particles undergoing primarily the electromagnetic interaction, such as photons and electrons, the hadronic calorimeter is used to induce energy losses in particles that were not stopped within the electromagnetic calorimeter. Those particles interact primarily via the strong interaction with a slower showering process. The calorimeter region extends up to a radius of about 4.2 m.

The outermost components of the ATLAS detector is the *muon spectrometer*. A separate system for muons is necessary as they interact only via ionisation processes with the calorimeters, not depositing their entire energy. The spectrometer comprises two muon chamber systems and a toroidal magnet system. While the purpose of the first chamber is a measurement of the muon track with high spatial resolution, the second one functions as a muon trigger with good time resolution. The muon trigger is essential for a quick identification of events including at least one muon in order to provide a hardware-based event selection (even before storing collected data). The magnet system again is used to bend the muon trajectories for a precise measurement of their momenta.

3.2.1. Triggers & Data Acquisition

Before it is possible to analyse physics processes detected with the ATLAS detector, the trigger and data acquisition (TDAQ) system [65] needs to process the data. The TDAQ system is responsible for receiving and interpreting the signals from the different components of the ATLAS detector and converting them into datasets which can then be further processed and analysed. With a design bunch spacing of about 25 ns for the LHC, the detectors are confronted with event rates of 40 MHz. In different stages of the TDAQ system, the rate of recorded events is greatly reduced before they are written to permanent storage. The intended data storage rate of ATLAS during Run II of the LHC is 1 kHz, meaning that just about 0.0025% of the produced data is stored for later analysis.

The first trigger level, known as the *Level-1* trigger system, is based solely on hardware information. It takes reduced-granularity information from the calorimeters and the muon systems into account and makes fast decisions whether to continue processing or discard an event. The calorimeter trigger searches for objects such as high-p_T electrons and photons, jets, taus decaying into hadrons, as well as large missing and large total transverse energy [66]. Additionally, electrons, photons and hadron and tau objects can be requested to be isolated which introduces requirements for the separation between energy deposits of different candidates (see also Section 3.3). A separate muon trigger system receives patterns of hit strips from the muon trigger chambers and identifies bunch crossings that produced a muon with high accuracy. The trigger searches for patterns consistent with high-p_T muons originating from the interaction regions. The Level-1 triggers reduce the event rate to about 100 kHz within a time span of a couple of microseconds.

Based on the Level-1 trigger decision, *regions of interest* are constructed which contain the event components that were part of the decision. A software-based processing farm, called the *High Level Trigger* system (HLT), then reduces the event rate further [67]. Within the regions of interest, the HLT system takes into account all parts of the detector: full information from the calorimeters and also tracking information from the inner detector. Trigger elements from the Level-1 trigger are refined: energy depositions in the calorimeters are only considered if they are consistent with tracks observed in the inner detector (unless the identified particle is not expected to leave tracks); isolation criteria and cuts on the momenta of the particles are tightened. After the HLT system, the event rate is reduced by a factor of 100 to about 1 kHz. Only then are the events completely reconstructed in every region of the phase space and stored in the permanent storage system. The data rate at this point still amounts to approximately 1.6 GB/s.

3.2.2. ATLAS Coordinate System

For defining kinematics, tracks etc. in reconstruction as well as in later analyses, ATLAS uses a common coordinate system. Its origin is defined to be at the interaction point in the centre of the detector. The z axis runs along the beam pipe. The x axis points towards the centre of the LHC ring with the y axis pointing upwards, towards the surface of the earth. The x-y plane extends perpendicular to the barrel construction of the detector; it is commonly referred to as the *transverse* plane. The transverse momentum p_T within the transverse plane is one of the three quantities used to describe the kinematics of particles within ATLAS. The particle's orientation within the transverse plane is described by the angle ϕ. The definition of ϕ follows the convention of spherical polar coordinates: it is defined to be $\phi = 0$ when the momentum points along the x axis.

The second angle of the polar coordinate system θ is parameterised by the *pseudorapidity*

$$\eta := -\ln\tan\left(\frac{\theta}{2}\right) \quad \text{with } \theta \in [0, \pi] \tag{3.1}$$

which describes the longitudinal component of the particle's momentum $p_L \equiv p_z$. As a function of the three-momentum $\boldsymbol{p}$, the pseudorapidity can also be expressed as

$$\eta = \frac{1}{2} \ln \left(\frac{|\boldsymbol{p}| + p_L}{|\boldsymbol{p}| - p_L} \right) = \operatorname{artanh} \left(\frac{p_L}{|\boldsymbol{p}|} \right). \tag{3.2}$$

In the ultra-relativistic limit where $E \approx p$, the pseudorapidity is identical to the definition of the rapidity y which is an additive quantity. This also implies that differences Δy in rapidities are Lorentz-invariant. To describe the distance between particles, a distance parameter R is introduced. It is defined as the distance of two objects in the η-ϕ plane

$$\Delta R := \sqrt{(\Delta\eta)^2 + (\Delta\phi)^2} \tag{3.3}$$

with $\Delta\eta = |\eta_1 - \eta_2|$ and $\Delta\phi = |\phi_1 - \phi_2|$ between the two objects.

3.3. Objects Definitions

Before analyses can be performed, the TDAQ system interprets the detector signals and converts them into datasets with actual physics objects, as described in Section 3.2.1. For that, fixed definitions of how to build physics objects such as electrons and muons from calorimeter deposits and tracks have to be applied. The following paragraphs will briefly describe how the objects are reconstructed.

Electrons are reconstructed from tracks in the inner detector associated with energy deposits, called *clusters*, in the EM calorimeter. For the identification, likelihood-based selection criteria are applied, described in detail in Ref. [68–71]. Within the analyses of this thesis, the tight identification requirements are chosen. Electrons are required to have a transverse momentum $p_T > 7\,\text{GeV}$ and $|\eta_{\text{cluster}}| < 2.47$. Due to the barrel/endcap transition in the EM calorimeter, deposits in the region $1.37 < |\eta_{\text{cluster}}| < 1.52$ have worse energy resolution. Therefore, electron candidates within this region are rejected.

The reconstruction of muons is based on track segments found in the layers of the muon spectrometer and corresponding tracks in the inner detector. They are required to have $p_T > 7\,\text{GeV}$, $|\eta| < 2.4$ and to pass the medium identification requirements described in Ref. [72]. If electron candidates share a track with muon candidates, they are removed.

To reduce fake contributions to both electrons and muons from non-prompt leptons, such as leptons originating from decays of heavy-flavour hadrons, isolation criteria are applied to both electrons and muons. To check isolation, the total sum of track transverse momenta around the track of the candidate is checked. Within a cone of radius r, defined as the minimum of $10\,\text{GeV}/p_T$ and a fixed radius parameter r_i, the total sum must be less than 6% of the candidate's transverse momentum. r_i is particle-dependent; it is chosen to be $r_e = 0.2$ and $r_\mu = 0.3$ for electrons and muons, respectively. Because the isolation criteria change for different values of p_T, this definition is also known as *gradient* isolation.

Additional requirements on the longitudinal and transverse impact parameters z_0 and d_0 are imposed to further increase isolation.

Jets are reconstructed using the anti-k_T algorithm [73] with a radius parameter of $R = 0.4$. Additional corrections accounting for the effect of pile-up on the jet energies as well as for energy-scale calibrations are applied to the jet objects. Their kinematics are required to fulfil $p_T > 25\,\mathrm{GeV}$ and $|\eta| < 2.5$.

Jets are assigned a b-tag weight depending on whether they are assumed to contain b-hadrons. This is achieved with the MV2C10 algorithm [74], a multivariate discriminant that takes various peculiarities of b-hadrons into account, such as their typical decay lengths within the detector. Above a certain threshold, also called the *working point* of the algorithm, jets are assigned a b-tag. The threshold is determined in such a way that the average efficiency to correctly assign a b-tag to a jet containing a b-hadron is 77%. This corresponds to an average rejection efficiency of light and gluon jets of about $(1 - 1/130) \approx 99.2\%$.

Neutrinos in physics processes cannot be detected, but they leave an imbalance in terms of the total transverse momentum of the corresponding event. The missing transverse momentum $\boldsymbol{p}_T^{\mathrm{miss}}$ with magnitude E_T^{miss} is calculated as the negative sum over all transverse momenta of electrons, muons and jets plus an additional soft term taking into account all other tracks originating from the primary vertex [75].

In a last step, called *overlap removal*, overlaps between physics objects are checked. Jets within $\Delta R < 0.2$ of electrons are entirely removed to avoid possible double-counting. To reduce non-prompt muons from heavy-flavour decays, muons are removed if they are closer than $\Delta R = 0.4$ to a jet object. If that jet object, on the other hand, has fewer than three associated tracks, the energy deposition of the jet might in fact originate from muon energy losses in the calorimeter due to its high energy. In that case, the jet is removed instead of the muon.

4. Reconstruction of $t\bar{t}Z$ Events

The ATLAS detector records a plethora of physics events, but, when trying to discover specific new physics processes, only a fraction of them is of interest. Although the $t\bar{t}Z$ signal was measured with an observed significance of 4.2σ and 6.4σ by the ATLAS and CMS collaborations in 2015, respectively [11, 60], its cross section has not been determined precisely yet. Beyond the ongoing analyses, an accurate reconstruction of the final state of $t\bar{t}Z$ events is essential to measure the coupling between the Z boson and the top quark. Only then would it be possible to measure or to set limits on the weak isospin of the top quark which eventually verifies or constrains the predictions of the Standard Model.

Another pivotal step for the observation of rare processes is the discrimination of the signal against background events. To optimise the signal-over-background ratio as well as the signal significance, not only a cut-based event selection, but also multivariate techniques are used. Sophisticated methods such as neural networks require event variables with separation power in order to enable an effective separation. Establishing a systematic way to reconstruct the final states of physics processes also introduces quantifiers of the reconstruction. These quantifiers can be used as additional separating variables.

The studies conducted for this thesis focus on the reconstruction of $t\bar{t}Z$ events using kinematic likelihood fits. In Section 4.1, the final state of $t\bar{t}Z$ events is discussed. The section focuses on the problems that become apparent when reconstructing them. Section 4.2 introduces kinematic likelihood fits as a systematic method to reconstruct final states. The section emphasises both the concept of kinematic likelihood fits as well as the tool *KLFitter* that is used for the studies of this thesis. Following that, Section 4.3 introduces the application of kinematic likelihood fits to the reconstruction of $t\bar{t}Z$ final states. The last section of this chapter, Section 4.4, describes the techniques used to evaluate the performance of the *KLFitter* reconstruction.

4.1. The Trileptonic $t\bar{t}Z$ Final State

The topology of $t\bar{t}Z$ events is identical to that expected in $t\bar{t}$ production with an additional Z boson in the final state. This Z boson decays either hadronically to a quark-antiquark pair ($q\bar{q}$) or leptonically to two charged leptons (l^+l^-) or two neutrinos ($\nu\bar{\nu}$). Since the decay to neutrinos results in imponderable kinematics because of the undetectable neutrinos, it is usually not considered for analyses. A hadronically decaying Z boson poses

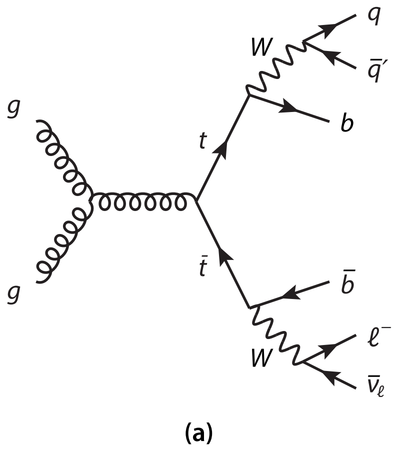

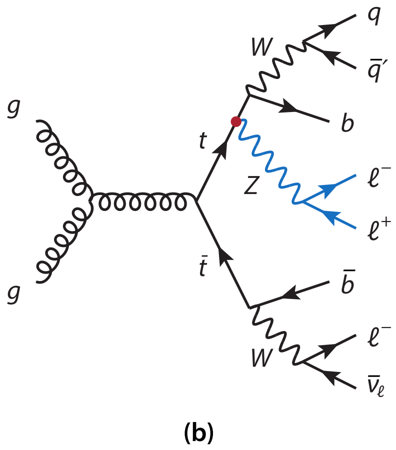

Figure 4.1.: Feynman diagrams of a) $t\bar{t}$ production in the lepton+jets channel and b) a trileptonic $t\bar{t}Z$ process. In both processes one top quark decays leptonically, the other one hadronically. The Z boson radiated from one of the top quarks decays to two additional charged leptons.

the problem of overwhelmingly dominating backgrounds: QCD-driven radiation of two additional jets is a very common process and the signature of a $t\bar{t}$ event with two additional jets is identical to that of a $t\bar{t}Z$ event with $Z \to q\bar{q}$. As a consequence, analyses in the $t\bar{t}Z$ sector are typically performed for the leptonic $Z \to l^+l^-$ decay only.

The remaining events are further divided according to the $t\bar{t}$ decay channels as explained in Section 2.2.3. The tetra-, tri- and dileptonic $t\bar{t}Z$ channels correspond to a $t\bar{t}$ pair in the dilepton, lepton+jets and all-hadronic channels, respectively.

The following reconstruction studies focus on the trileptonic channel, i.e. a $t\bar{t}$ pair in the lepton+jets channel with associated $Z \to l^+l^-$ production. A Feynman diagram of such a trileptonic $t\bar{t}Z$ process in comparison to $t\bar{t}$ production can be seen in Fig. 4.1. The final state of this process carries a complex signature of four jets, three leptons and a neutrino, only visible via missing transverse momentum. Out of the four jets, two are expected to be identified as b-jets (b_{lep} and b_{had}). The other two originate from *light* quarks, one from an up-type and the other from a down-type quark, to be precise. Out of the three leptons, two are anticipated to have the same flavour, but opposite charge.

The most challenging events in terms of reconstruction are those in which all three leptons are of the same flavour. The studies of this thesis focus on those events for which the following event selection is applied:

1. *Jets:* At least four jets are required with $p_T > 25\,\text{GeV}$ and $|\eta| < 2.5$.
2. *b-tagged jets:* No cuts on the number of b-tagged jets are applied.
3. *Leptons:* Exactly three leptons of the same flavour are required with a transverse momentum of $p_T > 25\,\text{GeV}$ for the highest-p_T lepton, $p_T > 20\,\text{GeV}$ for the other two

leptons. Muons have to fulfil $|\eta| < 2.5$. Electrons need to be within $|\eta| < 2.47$ and they are rejected in the region $1.37 < |\eta| < 1.52$ because of significantly lower reconstruction efficiencies in the EM calorimeter crack region. The number of leptons of the other flavour has to be zero.

The leptons are required to be *isolated* as well, in accordance with the isolation criteria introduced in Section 3.3. Moreover, depending on the flavour, either the muon or the electron trigger must have fired.

τ leptons cannot be measured directly due to their short lifetime. Consequently, events with $Z \to \tau\tau$ or with a top quark decaying to a tau are not detected as such. However, a fraction of τ leptons decays leptonically to muons via $\tau \to \nu_\tau \bar{\nu}_\mu \mu$ (or similarly to electrons). Consequently, these events are observed as events containing a muon (or electron).

4. *Neutrinos:* The only way to find events with neutrinos are checks of the missing transverse momentum. Generally, top quark analyses in the lepton+jets channel apply cuts on E_T^{miss}, requiring a missing transverse momentum above a threshold, such as $E_T^{\text{miss}} > 30$ GeV, to suppress background events without any neutrinos. For the following studies, however, no cuts on E_T^{miss} are applied to exploit the full range of available statistics.

To enable precise measurements of the properties of the top quarks and their coupling to Z bosons, it is critical to reconstruct them from their decay particles. The complication of this procedure is the level on which the actual observation takes place: the $t\bar{t}Z$ particles are produced on *parton level.* After their decays, the decay particles undergo processes such as hadronisation and parton showering; they form bound states or are subject to subsequent decays. This level is known as *particle level.* The detector, however, measures only energy deposits and tracks, ideally associated with each other. From these signals, particles and jet objects are constructed, as described in Section 3.3. This last level, at which the detection takes place, is hence also known as *detector level.*

Given the final state of a trileptonic $t\bar{t}Z$ event, which comprises four jets, three leptons and missing transverse momentum, there is no inherent way to "trace" those objects back to their origins. Thus, the primary process on parton level cannot be reconstructed naïvely from them. Even before reconstruction, the assignment of the observed objects to those of the parton level is beset with difficulties.

Taking combinatorics into consideration, any of the jets could be matched with any of the four quarks: the up-type and down-type quark (q_u and q_d) originating from the hadronic W boson, as well as the two b-quarks (b_{lep} and b_{had}). Additionally, any of the observed lepton candidates could be matched with any of the leptons on parton level. For a correct assignment in the trileptonic $t\bar{t}Z$ channel, a distinction between the up-type and down-type quark is not necessary as they both originate from the hadronic W boson. Furthermore, a separation between the two leptons arising from the Z boson decay is not required. This still allows 36 hypothetical assignments: $4!/2 = 12$ possibilities to match the jets to the quarks, and $3!/2 = 3$ to match the lepton candidates to the parton-level leptons.

By imposing additional constraints on kinematic variables, the number of highly probable assignments can be reduced. A common condition in searches for $t\bar{t}Z$ processes would be a requirement for an opposite-sign lepton pair with an invariant mass m_{ll} close to the mass of the Z boson, such as $|m_{ll} - M_Z| < 10$ GeV. Light jets and b-quark jets could be distinguished using b-tagging information and requiring two b-tagged jets in the final state. Although these constraints reduce background contributions and enable a distinction of the 36 possible assignments, they do not constitute a systematic method to decide about their quality.

Kinematic likelihood fits are one option to quantify the assignments systematically. They can be utilised to calculate assignment probabilities between detector-level and parton-level objects. The next section introduces underlying principles and techniques of the kinematic-likelihood fitting program *KLFitter* that will be used for reconstructing $t\bar{t}Z$ final states.

4.2. The *KLFitter* Package

One of the major problems in particle physics experiments is the accessibility of the primary physics processes. As described in the previous section, the partons produced in the interaction undergo several phenomena before detection and there is no inherent way to reconstruct parton-level objects based on the detector-level observations. Kinematic likelihood fits constitute a method to assign correctly the detected objects to partons systematically with high probability. The *KLFitter* package [12] which is based on the *Bayesian Analysis Toolkit (BAT)* [76] makes use of this reconstruction method. It is an acknowledged tool that has been used in several analyses, e.g. in Ref. [77–82].

Before going into more detail about the *KLFitter* package used to perform reconstruction studies within this thesis, the next subsection will briefly introduce the idea of kinematic likelihood fits.

4.2.1. Kinematic Likelihood Fits

The kinematic likelihood fits used within the *KLFitter* package are based on *Bayes' theorem*. Within the Bayesian interpretation in statistics, a probability $P(a)$ is often described as a “degree of belief” for a hypothesis a to be true. The Bayesian theorem associates the probability for this hypothesis with certain evidence b and provides a *conditional* probability $P(a|b)$:

$$P(a|b) = \frac{P(b|a)\,P(a)}{P(b)} \tag{4.1}$$

In Bayesian inference, the probability $P(a)$ is known as the *prior* probability before an observation of the evidence b. The expression $P(a|b)$ is referred to as the *posterior* probability, given that b has been observed. The function $P(b|a)$ to observe evidence b assuming a certain hypothesis a is known as the likelihood function. In many cases, the Bayesian theorem is also described as a "knowledge update": using additional evidence b leads to an updated probability distribution $P(a|b)$ compared to the prior distribution $P(a)$.

The concept of conditional probabilities is also used in kinematic likelihood fits. Kinematic properties such as the energies and momenta of detected particles are only known to a certain precision due to the detection methods. The relative energy uncertainty σ_E/E of a calorimeter decreases as the energy increases. Not considering electronic noise effects or leakage, the relative uncertainty scales with

$$\frac{\sigma_E}{E} \propto \frac{1}{\sqrt{E}}. \tag{4.2}$$

On the other hand, the resolution of momentum measurements in tracking detectors becomes worse as the momentum increases due to lower curvature for large momenta. The relative uncertainty of the momentum scales with

$$\frac{\sigma_{p_T}}{p_T} \propto p_T. \tag{4.3}$$

Taking these uncertainties in energy and momentum into account, the measured values $\tilde{E}_{\mathrm{meas}}$ can be related to the parton-level energies E_{true} of the underlying objects by parameterising these uncertainties. The corresponding functions are known as *transfer functions* $W(\tilde{E}_{\mathrm{meas}}|E_{\mathrm{true}})$. They describe the conditional probability for a reconstructed object to be measured with energy $\tilde{E}_{\mathrm{meas}}$ if the underlying parton-level object had the energy E_{true}.

Additionally, the energies of the reconstructed objects are constrained by the physical properties of the underlying partons, such as their masses or decay widths. For $t\bar{t}$ production with an associated Z boson, these constraining properties include the mass and the width of the top quark as well as those of the W and Z bosons. All these values have been measured in various experiments and (except for the top quark's decay width) are known with high precision. Considering the uncertainties parameterised by the transfer functions, these six quantities impose strong constraints on the reconstructed objects as well.

4.2.2. Event Reconstruction in *KLFitter*

The *KLFitter* package utilises both transfer functions for all reconstructed objects as well as constraints imposed by the known physical properties to perform event reconstruction.

KLFitter was originally designed to reconstruct the final state of the lepton+jets channel of $t\bar{t}$ production. The reconstruction objects are granted a certain variation of their energies according to the transfer functions $W(\tilde{E}_{\mathrm{meas}}|E_{\mathrm{true}})$. The expected top-quark and W-boson mass distributions impose additional constraints on the final-state reconstruction. The top quark's mass distribution is described by a Breit-Wigner function that is parameterised by the peak mass m_t and the decay width Γ_t:

$$B(x|m_t,\Gamma_t) \propto \frac{1}{(x^2 - m_t^2)^2 + (m_t\Gamma_t)^2} \tag{4.4}$$

The mass distribution of the W boson satisfies a similar distribution parameterised by m_W and Γ_W. In the lepton+jets channel of $t\bar{t}$, one W boson decays to two quarks, the other to a lepton and its neutrino. Thus, within the *KLFitter* package, the invariant mass of the q_u-q_d system and that of the l-ν_l system have to follow these $B(x|m_W,\Gamma_W)$ distributions, respectively. In a similar way, the reconstructed W bosons are paired with the b-quarks. Both the invariant masses of the W_{had}-b_{had} system and the W_{lep}-b_{lep} system have to follow the Breit-Wigner functions of the top quarks described in Eq. (4.4).

Combining all transfer functions with all Breit-Wigner distributions leads to the following likelihood function for the lepton+jets channel of $t\bar{t}$ production:

$$\begin{aligned}\mathcal{L} = {} & B(m_{q_1q_2q_3}|m_t,\Gamma_t) \times B(m_{q_1q_2}|M_W,\Gamma_W) \times B(m_{q_4l\nu}|m_t,\Gamma_t) \\ & \times B(m_{l\nu}|M_W,\Gamma_W) \times \prod_{i=1}^{4} W_{\mathrm{jet}}(E_{\mathrm{jet},i}^{\mathrm{meas}}|E_{\mathrm{jet},i}) \times W_l(E_l^{\mathrm{meas}}|E_l) \\ & \times W_{\mathrm{miss}}(E_x^{\mathrm{miss}}|p_x^{\nu}) \times W_{\mathrm{miss}}(E_y^{\mathrm{miss}}|p_y^{\nu}).\end{aligned} \tag{4.5}$$

As one neutrino is expected in the final state, its momentum components p_x and p_y are set in relation to the respective components of the missing transverse momentum $E_{x,y}^{\mathrm{miss}}$ via transfer functions as well. When performing the *kinematic likelihood fit*, *KLFitter* varies the energies of the *partons*, given the energies measured for the jet and lepton objects. The invariant masses are altered accordingly. The fitting procedure will be stopped once the likelihood value in Eq. (4.5) reaches a maximal value.

4.2.3. Deciding between Assignments

As mentioned in Section 4.1, there is no inherent way to find the correct assignment between parton-level and detector-level objects when performing event reconstruction. For $t\bar{t}$ events, the lepton+jets final state described by the likelihood in Eq. (4.5) expects four jets, one charged lepton and missing transverse momentum. Even if an event selection is applied that requires exactly four jets, there are still $4! = 24$ possibilities to assign the jets to the parton-level objects. As the up-type and down-type quark both come from the same W boson, they do not have to be distinguished. Nonetheless, this still leaves 12 permutations.

Within the *KLFitter* package, the kinematic likelihood fit is performed for *each* permutation separately. The resulting likelihood values can be used to quantify a reconstruction and to distinguish between the permutations. The idea behind this is the following assumption: the kinematic likelihood fit of a wrong assignment will lead to a lower likelihood value. On the one hand, the Breit-Wigner functions could be maximised. However, in order to reach the necessary invariant masses, the transfer functions would return very low values as the required energy shifts would be highly unlikely. On the other hand, the transfer functions could be maximised, yet this would cause the Breit-Wigner values to be small because the invariant masses would not reach the expected mass values.

For a better assessment of the returned likelihood values, they are normalised with respect to the sum over the likelihood values of all permutations. This quantity, the *event probability* p_i, also includes possible weighting factors Δp_i for the individual permutations i:

$$p_i = \frac{\mathcal{L}_i \Delta p_i}{\sum_j \mathcal{L}_j \Delta p_j} \tag{4.6}$$

Possible definitions of these weighting factors will be discussed in Section 4.3. In any case, whereas the likelihood value of a permutation is a simple quantifier of the reconstruction, the event probability sets the permutations in relation to each other. If one permutation stands out and returns a significantly higher likelihood value than all the others, its event probability will be close to 1. On the contrary, if two permutations have similar likelihood values, their event probabilities will be $p_i \lesssim 0.5$.

The *KLFitter* package performs kinematic likelihood fits for all possible permutations and calculates their individual likelihood values and event probabilities. The assignment with the highest event probability is then chosen to be the *best estimate* and will be returned as the reconstructed event.

4.3. Using *KLFitter* to Reconstruct $t\bar{t}Z$ Processes

KLFitter has been used in various analyses within top quark physics, the lepton+jets channel of $t\bar{t}$ production is only the most prominent one. The results presented in this thesis evaluate the performance of *KLFitter* in trileptonic $t\bar{t}Z$ events. In order to do that, several modifications and extensions were introduced to *KLFitter* to account for the expected $t\bar{t}Z$ final state. The following subsections will introduce the alterations that were implemented. They will also go into more detail about different options used within *KLFitter* to optimise its performance.

4.3.1. *KLFitter* Options for Jet Assignment

To optimise the performance of the final-state reconstruction, two different jet assignment modes are used within *KLFitter*. On the one hand, there is the *NoTag* method which takes the four leading-p_T jets as an input to the *KLFitter* reconstruction. The likelihoods and the event probabilities are calculated without any additional weighting factors Δp_i. Consequently, the best permutation in terms of the jet matching is decided only according to the kinematic information that the jets provide.

On the other hand, the second, more sophisticated *WorkingPoint* method takes b-tagging information of the jets into account. Again, the four leading-p_T jets are used for the reconstruction. To decide about the accuracy of the reconstruction, the *WorkingPoint* method, however, introduces weighting factors Δp_i. They are calculated using the b-tagging efficiencies ϵ_b and ϵ_l and the information about whether a jet was tagged as a b-jet:

$$\begin{aligned}\Delta p_i = &\begin{Bmatrix} \epsilon_b, & b_{\text{had}}\text{ tagged} \\ (1-\epsilon_b), & b_{\text{had}}\text{ not tagged} \end{Bmatrix} \times \begin{Bmatrix} \epsilon_b, & b_{\text{lep}}\text{ tagged} \\ (1-\epsilon_b), & b_{\text{lep}}\text{ not tagged} \end{Bmatrix} \\ &\times \begin{Bmatrix} \epsilon_l, & q_u\text{ tagged} \\ (1-\epsilon_l), & q_u\text{ not tagged} \end{Bmatrix} \times \begin{Bmatrix} \epsilon_l, & q_d\text{ tagged} \\ (1-\epsilon_l), & q_d\text{ not tagged} \end{Bmatrix}\end{aligned} \tag{4.7}$$

Whilst ϵ_b represents the probability to correctly identify a jet originating from a b-quark as a b-jet, the efficiency ϵ_l describes the probability to identify a jet as a b-jet when in fact it results from another parton. As introduced in Section 3.3, the information about whether a jet is tagged is provided by the MV2C10 algorithm. With the used working point of 77%, this results in $\epsilon_b \approx 77\%$ and $\epsilon_l \approx 1/130 = 0.77\%$ (determined via Monte-Carlo simulations).

The event probability of individual assignments is greatly affected when b-tagging information is taken into account. As chances to accidentally assign a b-tag to a jet originating from a light quark are very low, all permutations with a b-tagged jet at the position of q_u or q_d will have a considerably lower event probability. Not assigning a b-tag to a jet originating from a b-quark, however, is still possible in about 23% of the cases. Therefore, permutations with b-tagged jets at the positions of b_{had} and b_{lep} will be favoured, but non-tagged jets at these positions are not entirely rejected.

4.3.2. *KLFitter* Options for Lepton Selection

As three leptons, possibly of the same flavour, are anticipated in the trileptonic $t\bar{t}Z$ final state, several lepton assignment options within *KLFitter* were tested. The first tested method is the *Leading* mode. It continues to use the likelihood for the $t\bar{t}$ lepton+jets channel introduced in Eq. (4.5) and takes the leading-p_T lepton to reconstruct the leptonically decaying top quark. The two sub-leading leptons are assumed to originate from the Z boson decay and are not taken into account in the likelihood calculation. This method is merely used for comparison reasons as it is the standard lepton selection mode for the $t\bar{t}$ lepton+jets channel.

In the second method, the *AmongThree* mode, checks of the invariant masses of lepton pairs are performed. For all three lepton pairs of the three reconstructed leptons l_1, l_2 and l_3, the invariant mass $m(l_i, l_j)$ and its difference to the Z boson mass

$$\left| m(l_i, l_j) - M_Z \right| \tag{4.8}$$

are calculated. The pair with the smallest difference to M_Z is believed to be the pair originating from the Z boson, whereas the third one is used to reconstruct the $t\bar{t}$ topology. Once more, this method utilises the lepton+jets likelihood and does not perform any fit of the two leptons from the Z boson.

The third method, called the *Dedicated* mode, fully accounts for all particles in the trileptonic final state and performs a full fit for all of them. This method uses a dedicated likelihood function in *KLFitter*, which will be introduced in the next section.

4.3.3. Dedicated Likelihood for $t\bar{t}Z$ Events

Following the example of the likelihood for the lepton+jets channel introduced in Eq. (4.5), a dedicated likelihood for trileptonic $t\bar{t}Z$ events is introduced. Starting from the lepton+jets case, the likelihood is extended to account for the additional Z boson and its decay to two charged leptons. The extension includes transfer functions for the two leptons as well as a function that describes the expected distribution for the invariant mass of the two leptons.

The problem with parameterising this invariant mass distribution is the fact that the production of a lepton pair is not only possible via Z bosons, but also through γ processes. These two production modes interfere, causing additional terms in the theoretical description. Neglecting these interference terms, the production of two leptons via neutral weak currents is described by a Breit-Wigner distribution parameterised by the mass m_Z and the decay width Γ_Z of the Z boson.[1] The probability to produce a lepton pair via

---

[1] A few words of caution: in contrast to the implementation of the $t\bar{t}$ lepton+jets likelihood in *KLFitter*, the Breit-Wigner distributions in the $t\bar{t}Z$ implementation are *normalised*. This step is necessary for the introduced weighting between on-shell and off-shell terms. Hence, distributions of the likelihood

γ exchange is represented by a $1/m_{ll}^2$ distribution where m_{ll} is the invariant mass of the two leptons.[2]

As those two production modes cannot be separated, a mixture of both is used to describe the expected invariant-mass distribution. A fraction f_{on} is introduced as a weighting factor between these two functions. Consequently, the dedicated $t\bar{t}Z$ likelihood reads:

$$\begin{aligned}\mathcal{L} \;=\;& B(m_{q_1q_2q_3}|m_t,\Gamma_t)\times B(m_{q_1q_2}|M_W,\Gamma_W)\times B(m_{q_4l\nu}|m_t,\Gamma_t)\\ &\times B(m_{l\nu}|M_W,\Gamma_W)\times\prod_{i=1}^{4}W_{\text{jet}}(E_{\text{jet},i}^{\text{meas}}|E_{\text{jet},i})\times W_l(E_l^{\text{meas}}|E_l)\\ &\times W_{\text{miss}}(E_x^{\text{miss}}|p_x^{\nu})\times W_{\text{miss}}(E_y^{\text{miss}}|p_y^{\nu})\\ &\times W_l(E_{l_2}^{\text{meas}}|E_{l_2})\times W_l(E_{l_3}^{\text{meas}}|E_{l_3})\\ &\times\left[f_{\text{on}}\cdot B(m_{l_2l_3}|m_Z,\Gamma_Z)\;+\;(1-f_{\text{on}})\cdot\left(\frac{c_{\text{norm}}}{m_{l_2l_3}^2}\right)\right]\end{aligned} \tag{4.9}$$

To ensure a correct weighting between the two functions, they are both individually normalised to unity. In order to avoid the singularity for $m_{ll}\to 0$, a lower cut-off c_{cut} for the $1/m_{ll}^2$ contribution is added. Imposing the integral from c_{cut} to infinity to be equal to 1, the normalisation factor is determined to be $c_{\text{norm}}\equiv c_{\text{cut}}$.

Both the weighting factor f_{on} and the lower cut-off value c_{cut} are chosen in accordance with the parton-level mass distributions observed in the Monte-Carlo samples. The weighting factor is determined by the observed fraction of on-shell events in the distribution. The samples used are introduced in Section 4.4.1. The choice of the two parameters will be discussed in Section 4.4.2. Within the following sections, the non-on-shell contributions, including production via γ^* and γ^*/Z interference will be labelled as *off-shell*. It should be kept in mind that these labels *on-shell* and *off-shell* are sheer technical distinctions.

4.4. Evaluating the Performance of *KLFitter*

To evaluate the accuracy of the *KLFitter* reconstruction and test the impact of the introduced alterations and extensions, the *KLFitter* output has to be matched with the parton-level information. This section introduces the steps necessary to calculate reconstruction efficiencies, how the simulation of the events is performed and how the matching is evaluated.

The reconstruction algorithms are applied to Monte-Carlo samples, both for $t\bar{t}Z$ processes as well as expected background processes. Additionally, *KLFitter* is tested on $t\bar{t}$ sam-

---

output are not directly comparable to that of other *KLFitter* likelihoods.

[2] Within the Feynman calculus that is used to compute the cross sections of particle physics processes, the $1/m_{ll}$ term originates from the *propagator* of the photon.

ples to compare its performance for $t\bar{t}Z$ processes to that of the lepton+jets channel. The Monte-Carlo generators used for the individual samples are introduced in Section 4.4.1.

To check whether the reconstructed final state matches that of the parton level, the output of the analysis software has to allow easy access to the parton level. Several alterations are made to integrate information about the Z bosons and their decays into the parton-level output of the analysis software. The necessary steps are explained in Section 4.4.2. To perform the matching process between parton level and reconstruction, another software package, the *NtupleReader*, is introduced. The matching procedure and the package's functionality are described in Section 4.4.3.

4.4.1. Simulation of Events

For the following studies, Monte-Carlo simulation samples are used to model $t\bar{t}Z$ events. For additional studies, diboson samples consisting of $4l$, $lll\nu$ and $ll\nu\nu$ production as well as $t\bar{t}$ events are generated, too. Heavy-flavour decays involving b-quarks and c-quarks are modelled using the EVTGEN software [83]. The top quark mass is set to 172.5 GeV within all the generators. To simulate the response of the detector components of the ATLAS detector, the software package GEANT4 [84, 85] is used. All Monte-Carlo samples are processed using the *AnalysisTop* reconstruction software that is also used for data processing.

To investigate possible reconstruction differences, $t\bar{t}\mu^+\mu^-$ events are generated on two different levels of calculation. On the one hand, they are produced at leading order with multi-leg extension[3] using the matrix-element generator MADGRAPH5_aMC@NLO [57]. It is interfaced to PYTHIA8 [86] for the simulation of the showering processes. On the other hand, a next-to-leading order $t\bar{t}\mu^+\mu^-$ sample is produced with the aMC@NLO generator, also interfaced to PYTHIA. The contributions of γ^* and γ^*/Z interference are included in both samples. For the event generation, both samples utilise the A14 tune [87] conjointly with the NNPDF2.3 PDF set [43]. The leading-order sample is normalised to the $t\bar{t}Z$ cross section at NLO in QCD using k-factors [88].

Diboson processes including WW, WZ and ZZ in the respective channels $ll\nu\nu$, $lll\nu$ and $4l$ are simulated using the SHERPA 2.1 generator [89]. $t\bar{t}$ processes in the lepton+jets and dileptonic channel are generated using NLO matrix elements in POWHEG [90–92] and the CT10 PDF set [93]. The parton shower is simulated with the PYTHIA6 shower generator [94] in combination with the CTEQ6L1 PDF set [95] and the PERUGIA2012 tune [96].

---

[3] In case of the $t\bar{t}Z$ sample, multi-leg extension means that events are generated with up to one additional parton in the matrix elements.

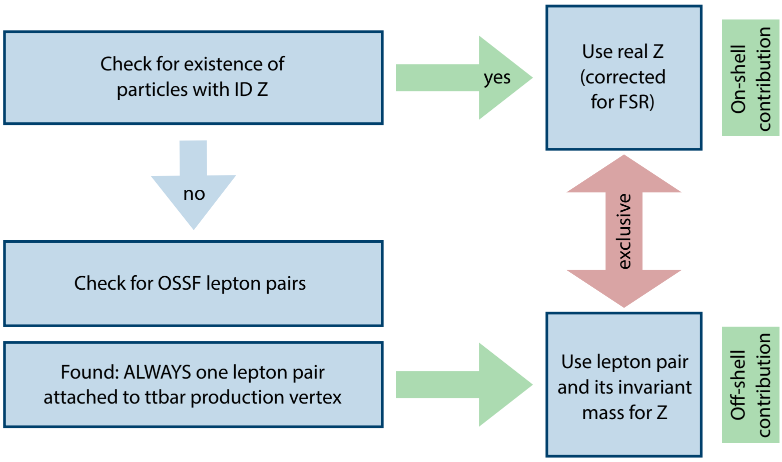

Figure 4.2.: Schematic of how the information about the Z boson and its decay products were collected from the truth record. The schematic also shows the difference of the on-shell and off-shell contributions.

4.4.2. Adjustment of the Truth-Record Output

To provide easy access for the matching, the output of the parton level had to be adjusted for $t\bar{t}Z$ events. Although this level of information, called the *truth record*, did provide information of all generated objects, the Z boson and its decay products had to be easily accessible to evaluate the *KLFitter* performance. In the corresponding package of the analysis code, an implementation for $t\bar{t}$ events was already provided, therefore it was only necessary to add a method to save information about the Z boson. By scanning the truth record for particles labelled[4] with ID = 23, it was determined that only a certain fraction of the events contained such a particle. Therefore, two different methods were applied to cover all events. A schematic of the applied methods can be seen in Fig. 4.2.

For events containing a particle with ID = 23, this particle was traced back to its origin and it was found that it is always – as expected – radiated by a top quark. Therefore, those particles were saved as the presumed Z bosons, whereas their two decay products were cross-checked to be a lepton pair of same flavour, but opposite sign, and then saved as well.[5] These events correspond to the contribution of on-shell Z bosons with the characteristic Z mass peak.

On the other hand, the produced samples contain events with no particle with ID = 23. By examining the mass distributions, it was found that those events account for all contributions labelled as *off-shell*, such as pure γ^* processes, production via highly virtual Z^* bosons and γ/Z^* interference. In all cases, they were found to contain a lepton pair

---

[4] Within Monte-Carlo generators, particles are labelled according to an identification system known as PDG ID. The Z boson has the identification number 23.

[5] Within the truth record, the state of the particles is altered several times due to virtual corrections. The saved state corresponds to the state right before the particle's decay.

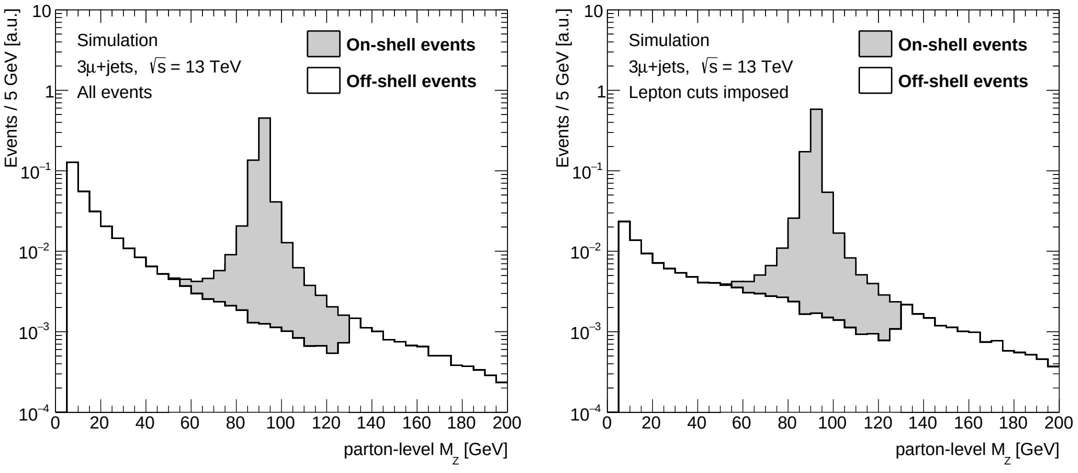

(a) (b)

Figure 4.3.: Invariant-mass distribution of the two leptons on parton level for a) all events and b) events that pass the imposed lepton cuts described in Section 4.1. The plots show both the on-shell events following a Breit-Wigner distribution and the events labelled as off-shell.

with same flavour, but opposite sign which is directly attached to the $t\bar{t}$ production vertex. This is not to be interpreted as an actual physical production at that vertex, but rather it is an artefact of how the associated production is modelled within the Monte-Carlo generators. For those events, the sum of the four-momenta of the two leptons was saved as the off-shell Z boson; the leptons themselves were saved as the decay products.

Figure 4.3 shows the observed mass distributions on parton level for both on-shell and off-shell events within the NLO $t\bar{t}Z$ sample. Stacked on top of each other, the two types of events show a smooth distribution. The figure also includes the mass distribution after imposing the cuts on the lepton kinematics introduced in Section 4.1. The fraction of events towards the lower end of the mass scale is significantly reduced.

From the observed distributions, the likelihood parameters f_{on} and c_{cut} were determined. The fraction of on-shell events was found to be $f_{\mathrm{on}} = 0.8690 \pm 0.0020$ when considering the imposed lepton cuts. As seen in the figure, the parton-level mass distribution includes a sharp cut-off. Consequently, the cut-off value for the dedicated likelihood (and therefore also the normalisation factor c_{norm}) was chosen to be $c_{\mathrm{cut}} = 5\,\mathrm{GeV}$.

4.4.3. Matching Parton Level and Reconstruction

To evaluate the accuracy of the *KLFitter* reconstruction, its output has to be compared to parton-level information. For this step, the software package *NtupleReader* was created. Results of the comparison will be discussed in the next chapter.

NtupleReader compares the parton-level information to the reconstruction output considering the chosen assignment by *KLFitter*. In a first step, the presence of the four expected quarks (b_{lep}, b_{had}, q_u, q_d) is checked. It is tested whether a jet is present within a radius of $R = 0.3$ around the quarks in the η-ϕ space. If there is an object present, the respective quark is tagged *IsPresent*. If multiple objects are present, it receives an additional *Multimatch* tag. The whole event is called *UniqueMatch* when none of the quarks has acquired such a tag. Provided jets are found for all four quarks and those jets are among the four highest-p_T jets of the event, the event is labelled *AllJetsWithinFour*. This constitutes an important qualifier of the *KLFitter* reconstruction as only the four highest-p_T jets are taken into account in both tested jet selection modes (see Section 4.3.1).

In a second step, the correct association of jets and quarks is evaluated. Not only does *NtupleReader* now require an object close to the quark, but also it checks whether the assignment matches the object on parton level. Given that the assignment is correct, the quark is assigned the tag *IsMatched*.

In a similar manner the lepton presence and matching is evaluated. Given a reconstructed lepton is within a radius of $R = 0.1$ around the parton-level lepton, it receives the tag *IsPresent*. Additionally, if the lepton is assigned correctly to the corresponding object on parton level, it is labelled as *IsMatched*.

Moreover, the assigned reconstruction objects are combined in order to recreate the four-momenta of their mother particles. The matching between those reconstructed four-momenta with the corresponding truth-record partons is also checked. The W_{had} boson receives the tag *Matched* when both light quarks are correctly associated.[6] Furthermore, the four-momenta of the two top quarks are calculated by adding the four-momenta of their respective decay products – both on reconstruction and parton level. If the reconstructed top quarks are within a radius of $R = 0.4$ around the parton-level top quarks, the hadronic and leptonic top quark receive the tags *THadMatched* and *TLepMatched*, respectively.

By measuring the fraction of events that contain these tags, matching efficiencies can be calculated and the *KLFitter* reconstruction performance can be assessed. These evaluation steps are done for all *KLFitter* modifications described in Section 4.3 including combinations of the different jet and lepton selection modes. Furthermore, $t\bar{t}$ production in the lepton+jets channel is used as a benchmark to rank the performance for $t\bar{t}Z$ events. For those runs, only the original lepton+jets likelihood is used with different jet selection modes. The cuts introduced in Section 4.1 are changed to exactly one lepton, i.e. either $N_\mu = 1$ or $N_e = 1$. *KLFitter* is then set to use this lepton for the leptonic top quark.

---

[6] Since up-type and down-type quark originating from the W boson are not distinguished in the used *KLFitter* setup, the only requirement is that both light jets are matched to the light quarks.

5. Performance Results

In the previous chapter, the final state of $t\bar{t}Z$ events was discussed, the reconstruction of which comes with combinatorial difficulties. *KLFitter* was introduced as a tool to perform kinematic likelihoods in order to reconstruct final states of particle physics processes systematically. After a general description of the calculation steps, the chapter put an emphasis on the alterations and extensions to the *KLFitter* package that were used to design a systematic $t\bar{t}Z$ reconstruction. Different lepton and jet modes were proposed and methods to evaluate the reconstruction efficiencies were reviewed.

This chapter presents the results of the reconstruction studies. In Section 5.1, the introduced lepton and jet modes are compared and their performances evaluated using the tool *NtupleReader* introduced in the previous chapter. Section 5.2 focuses on the jet matching efficiencies of the different modes. A comparison of the $t\bar{t}Z$ reconstruction to the performance of *KLFitter* for $t\bar{t}$ processes will be shown in Section 5.3. The next section then focuses on studies concerning the design of the dedicated likelihood. Its efficiencies will be compared to the reconstruction of likelihoods that solely account for on-shell and off-shell contributions. Following that, Section 5.5 discusses the possibility to use the likelihood output of *KLFitter* as a separation variable to discriminate signal and background events.

5.1. Comparing Jet and Lepton Modes

In the last chapter, different methods to assign the jets to the partons were introduced. Additionally, different approaches to deal with the three expected leptons were discussed. The impact of those different methods will be presented within this section based on NLO $t\bar{t}\mu^+\mu^-$ Monte-Carlo simulations. In order to allow a correct matching within *KLFitter*, the four anticipated jets of the $t\bar{t}Z$ final state have to be the four highest-p_T jets as only those jets are considered within the reconstruction algorithm.[1] Consequently, this section will only cover events that were labelled as *AlljetsWithinFour* and *UniqueMatch*. This correponds to a fraction of approximately 13.8% of the events that passed the selection.

In Fig. 5.1, a comparison of different jet and lepton modes used for the *KLFitter* recon-

---

[1] In case one of the four expected jets is not among the four highest-p_T jets of an event, the *KLFitter* algorithm will perform the reconstruction with the incorrect set of jets. A *UniqueMatch* tag implies that none of the expected final-state partons is matched to multiple detected objects.

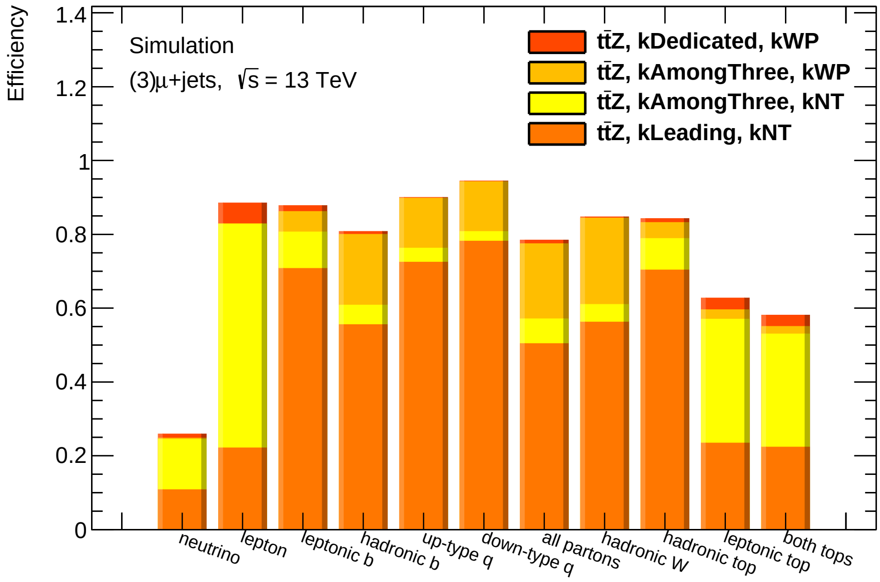

Figure 5.1.: Matching efficiencies for different lepton and jet modes as described in Section 4.3. The *AmongThree* mode shows notable enhancements for lepton, neutrino and b_{lep}. Including b-tagging information with the *WorkingPoint* mode improves the efficiencies for all four jets significantly. The dedicated likelihood in the *Dedicated* mode results in another efficiency gain for the lepton reconstruction. Statistical uncertainties, which are all below 1%, are not displayed to maintain clarity of the plot.

struction can be seen. The lepton modes comprise *Leading* that utilises the lepton+jets likelihood of $t\bar{t}$ and takes the leading-p_T lepton, *AmongThree* which introduces a comparison of m_{ll} to the Z boson peak mass, and *Dedicated* with a dedicated $t\bar{t}Z$ likelihood. For the jet assignment, the two modes *NoTag* and *WorkingPoint* were used. While the first one does not introduce any permutation-specific weights, the latter one takes b-tagging information for the jet assignment into account. The diagram shows the matching tags for the individual partons as discussed in Section 4.4.3.

A comparison of the lepton selection mode *AmongThree* with *Leading* shows a significant performance improvement for the matching of the lepton from 22.2% to 82.9%, which corresponds to an increase of more than 270%. That is expected as *Leading* considers the leading-p_T lepton to be the lepton from the leptonically decaying top quark although the p_T is not a quantity that inherently allows a distinction of the three final-state leptons. Additionally, a significant improvement of the matching of b_{lep} can be seen: using a wrongly assigned lepton increases the chance that *KLFitter* also incorrectly assigns the jet objects in order to reach the anticipated W boson and top quark masses in the Breit-Wigner distributions (see Eq. (4.9)). Consequently, the reconstruction efficiencies for all other partons are improved when using the *AmongThree* mode.

Furthermore, the diagram shows a remarkable increase of the neutrino matching with the *AmongThree* mode which can be explained with the mass distribution of the leptonic W boson. The small width Γ_W of the Breit-Wigner distribution implies strong correlations between the kinematics of the lepton and the neutrino. Therefore, an incorrect choice of the lepton causes the reconstruction of the neutrino to fail as well with high probability. Improvements of the reconstruction of all three objects on the leptonic branch lead to a notable efficiency increase for the leptonic top quark itself.

Comparing the reconstruction efficiency of the *NoTag* with the *WorkingPoint* mode, the latter leads to an increase of multiple efficiencies as well. By introducing weights for the individual permutations that include b-tagging information of the jet objects, the reconstruction of all four quarks is enhanced by an average of 10%. As shown in Eq. (4.7), the weights used are calculated with the b-tagging efficiencies ϵ_b and ϵ_l for jets originating from b-quarks and non-b-quarks, respectively. Using the efficiencies ϵ_i or $(1-\epsilon_i)$ for all four jet objects that are assigned to the quark positions, a joint probability for each assignment is calculated. Therefore, *KLFitter* strongly favours permutations which assign b-tagged jets to b_{lep} or b_{had} while having non-tagged jets matched with q_u and q_d. With a better reconstruction of all four quarks, the hadronic W boson and the hadronic top quark are reconstructed with higher efficiency as well.

Introducing a dedicated likelihood for $t\bar{t}Z$ events with the *Dedicated* mode leads to another performance optimisation when compared to the *AmongThree* mode. In particular, the probability to correctly reconstruct the lepton of the $t\bar{t}$ topology is increased by approximately 5%. This leads to slight improvements of the reconstruction of all other partons. As a consequence, the efficiencies of the reconstruction of t_{lep} and both top quarks combined are improved by about 2%.

5.2. Efficiencies of Jet Matching

It was shown in the previous section that the jet matching efficiencies of the *NoTag* and the *WorkingPoint* mode differ considerably due to the b-tagging information included in the calculations. These efficiencies were also examined for *all* selected events, without requiring events to be labelled *AllJetsWithinFour* and *UniqueMatch*. The efficiencies were probed using matching matrices that display a mapping between the partons and the true origins of their matched objects. Matrices for both jet assignment modes are presented in Fig. 5.2.[2] As up-type and down-type quarks are not distinguished in the used likelihoods, they are shown as correctly matched as soon as the corresponding jets are assigned to either of them.

Overall, the *WorkingPoint* mode shows a substantially better performance for all four jets as seen on the diagonal of the matrices. The fraction of correctly matched light jets

---

[2] A separate comparison for the *Leading* and *AmongThree* lepton modes can be found in Fig. A.1 in the appendix. The displayed matrices both use the *NoTag* jet assignment modes.

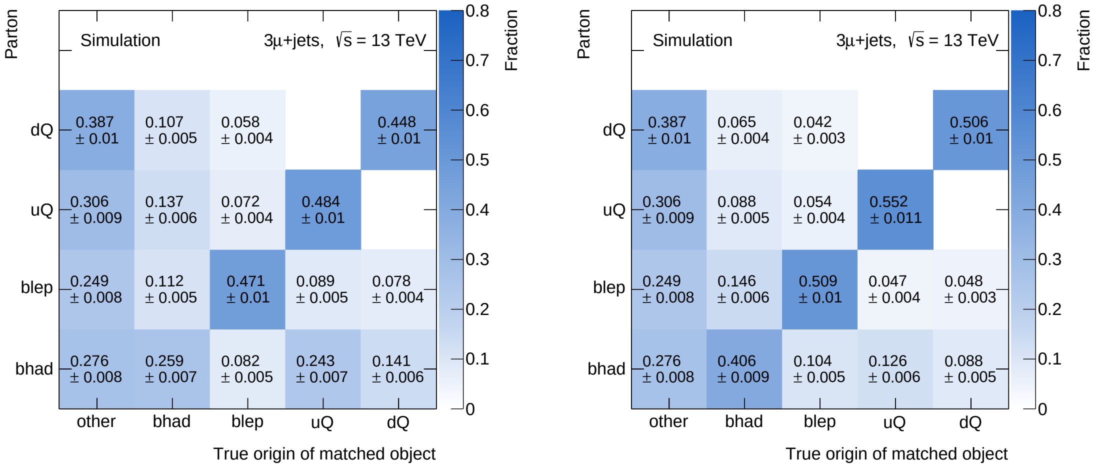

(a) (b)

Figure 5.2.: Jet matching matrices for NLO $t\bar{t}Z$ events for a) the *NoTag* and b) the *WorkingPoint* mode described in Section 4.3.1. The matrices map the partons to the true origin of their matching partners. When comparing the diagonals of the matrices, the *WorkingPoint* mode shows a significantly better performance due to the included b-tagging information.

increases by about 5% each, with the efficiency for b_{had} up by almost 15%. For the *NoTag* mode, the b_{had} is matched erroneously to the object originating from the up-type quark in almost 25% of the events and therefore stands out among the off-diagonal elements by about 10%. This effect becomes negligible for the *WorkingPoint* mode as the determined fraction of 12.6% is in the same range as the other off-diagonal elements. The left-most column displays the fraction of events for which the partons are not matched to any of the four anticipated jets originating from the $t\bar{t}Z$ final state. It can be seen that the two jet assignment modes do not have any impact on the fraction as they do not change the way the jets are selected before fitting.

5.3. Performance for $t\bar{t}$ and $t\bar{t}Z$

The discussed NLO simulations of $t\bar{t}\mu^+\mu^-$ events were also compared to LO Monte-Carlo simulations with multi-leg extension. To better assess the performance of *KLFitter* for both of them, $t\bar{t}$ events generated at NLO were reconstructed as well. As discussed in Section 4.4.3, the event selection for $t\bar{t}$ was changed to exactly $N_\mu = 1$ to fit the anticipated number of leptons in the lepton+jets channel.

A similar comparison plot to that in Fig. 5.1 can be found in Fig. 5.3. Again, only events with the two labels *AllJetsWithinFour* and *UniqueMatch* are considered. This provides the *KLFitter* algorithms with similar prerequisites for both types of process – despite their

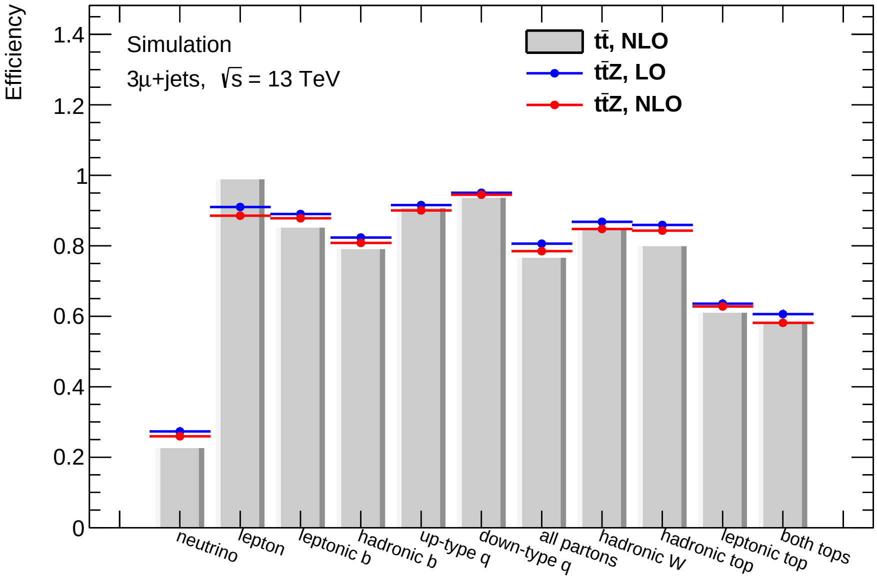

Figure 5.3.: Matching efficiencies for LO and NLO simulations of $t\bar{t}Z$ processes and NLO $t\bar{t}$ processes. Both types of events were reconstructed using their respective dedicated likelihoods and the *WorkingPoint* jet assignment mode. For all partons except for the lepton, both $t\bar{t}Z$ simulations are reconstructed with higher efficiencies. Statistical uncertainties on the efficiencies are below 1% and not displayed to maintain clarity.

different final states and complexity. The diagram displays the performance with the *Dedicated* and *WorkingPoint* modes for both the LO and NLO $t\bar{t}Z$ samples. Additionally, they are compared to the performance for $t\bar{t}$ events using the *WorkingPoint* mode.

The diagram shows an overall comparable performance for both processes. As expected, the lepton matching efficiency in $t\bar{t}$ processes is close to 1 since the event selection only chooses events with exactly one lepton. All other partons are reconstructed with similar or higher efficiencies for $t\bar{t}Z$ events. This also leads to improvements in the combined variables, such as the two top quarks. Among the two levels of $t\bar{t}Z$ simulation, the reconstruction is slightly more efficient for the LO Monte-Carlo sample. Significant differences can mainly be found in the leptonic branch, such as in the matching efficiencies of the lepton and b_{lep}.

To evaluate possible differences in the matching of the jets, matrices, equivalent to those introduced in the previous section, are compared as well. The matrices for $t\bar{t}Z$ and $t\bar{t}$ at NLO are shown in Fig. 5.4. They both use the *WorkingPoint* jet assignment mode.[3] $t\bar{t}Z$ shows a higher fraction of events where the partons are not matched with any jet originating from the anticipated final state. Consequently, these jets must originate from additional objects radiated during the $t\bar{t}Z$ production; they are often called “extra jets”.

---

[3] A separate comparison of the jet matching for $t\bar{t}Z$ and $t\bar{t}$ using the *NoTag* jet assignment mode is made in Fig. A.2. The matrices of $t\bar{t}Z$ at LO and NLO are compared in Fig. A.3.

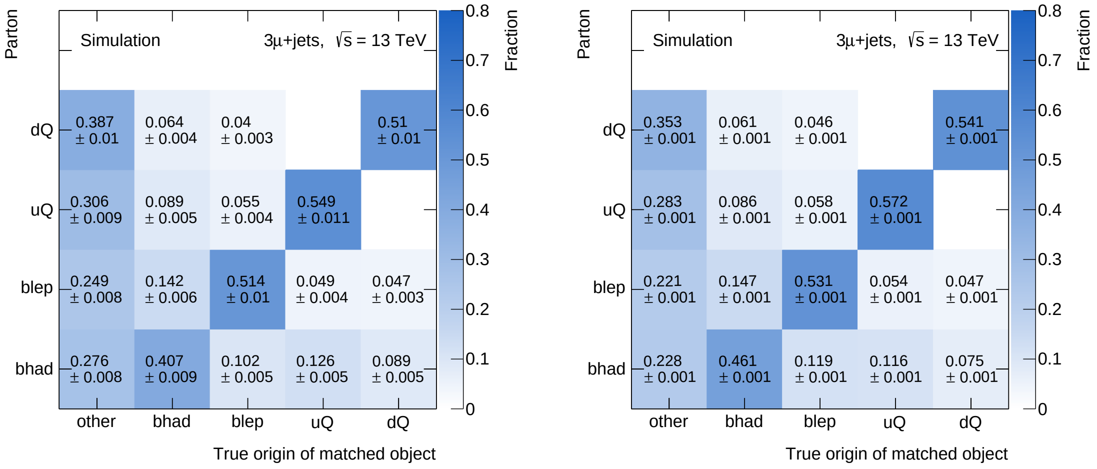

(a) **(b)**

Figure 5.4.: Jet matching matrices for the NLO Monte-Carlo simulations of a) $t\bar{t}Z$ and b) $t\bar{t}$ events. Both types of events are processed using their respective dedicated likelihoods and the *WorkingPoint* jet assignment mode. The $t\bar{t}Z$ matrix shows a higher fraction of events where partons are matched to jets originating from objects not anticipated in the $t\bar{t}Z$ final state ("extra jets").

Due to the higher proportion of unmatched partons the diagonal elements of the $t\bar{t}Z$ matrix are between 2% and 5% lower than the elements of the $t\bar{t}$ matrix. Apart from that, the fraction of partons that are accidentally matched with a jet from another parton of the final state is not significantly different.

In order to find possible explanations for the observed jet matching behaviour, the jet kinematics of the different simulations were compared. Figure 5.5 shows the jet multiplicity for $t\bar{t}Z$ at LO and NLO in comparison with $t\bar{t}$. Whereas no significant difference can be seen between the LO $t\bar{t}Z$ sample and $t\bar{t}$, the NLO simulation shows a different distribution compared to the other two. On average, $t\bar{t}Z$ events at NLO have a higher jet multiplicity than the LO simulation. This behaviour is expected: as higher orders of calculation are included in the Monte-Carlo generation of the events, more events with initial-state or final-state radiation are simulated. These "extra jets" lead to an – on average – increased number of jets per event. The difference between the NLO simulations of $t\bar{t}Z$ and $t\bar{t}$, however, cannot be explained and could be an artefact introduced by the two different generators used for $t\bar{t}Z$ and $t\bar{t}$.

Comparisons of the transverse momenta of the jets reveal noteworthy differences between $t\bar{t}Z$ and $t\bar{t}$. In the following, the jets of an event will be sorted according to their p_T values, e.g. the jet with the highest transverse momentum will be labelled as "first

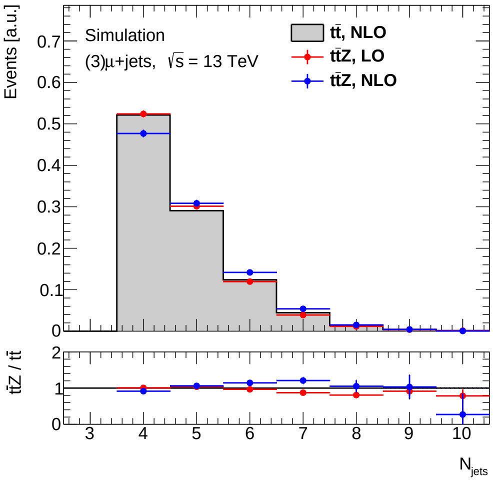

Figure 5.5.: Comparison of the jet multiplicities of LO and NLO $t\bar{t}Z$ processes to those of NLO $t\bar{t}$ processes. Both types of events were reconstructed using their respective dedicated likelihoods and the *WorkingPoint* jet assignment mode. The LO $t\bar{t}Z$ sample shows slight, but no systematic deviations from the $t\bar{t}$ data. NLO events tend to have a larger number of jets than $t\bar{t}$ events.

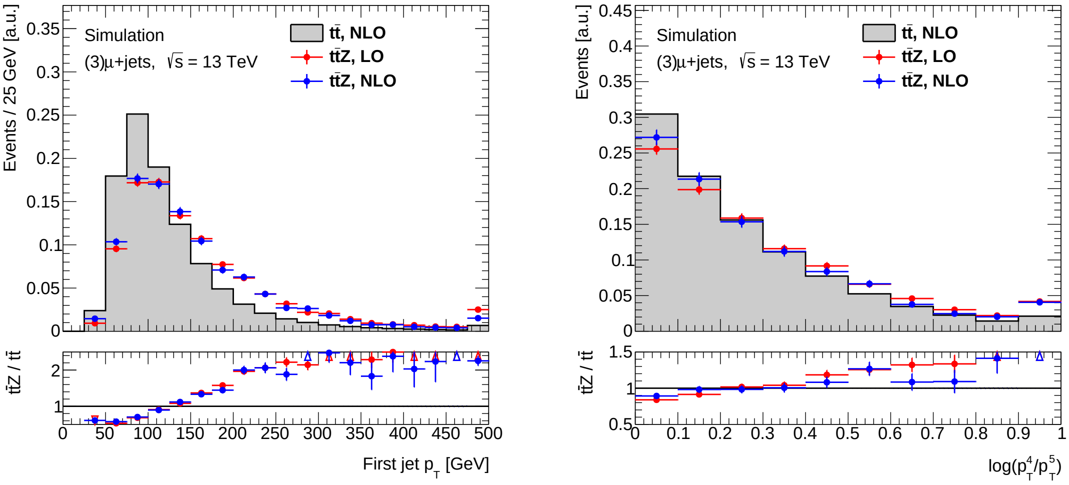

(a) **(b)**

Figure 5.6.: Comparison of the jet kinematics of $t\bar{t}Z$ and $t\bar{t}$ processes. Both were run with the *WorkingPoint* method, i.e. $t\bar{t}Z$ corresponding to method 3 described in Section 4.3. a) shows the p_T of the leading jet where the percentage of high-p_T jets is much greater for $t\bar{t}Z$ processes. b) displays the logarithmic ratio of the transverse momenta of the fourth and the fifth jet of events (containing five or more jets). The ratio reveals $t\bar{t}$ processes to have a higher probability for that ratio to be close to 1.

jet”. In Fig. 5.6a, the transverse momenta of the first jets are compared. Whereas the two $t\bar{t}Z$ simulations do not show any systematic differences, the ratio plot displays a strong discrepancy to $t\bar{t}$: on average, the p_T of the first jet is significantly higher for $t\bar{t}Z$ events. A similar behaviour is observed for all other jets as well. The corresponding plots for the second, third, fourth and fifth jet (if existing) can be found in Fig. A.5 and Fig. A.6 in the appendix. This observation could be caused by the differences in the $t\bar{t}Z$ and $t\bar{t}$ final states: the radiation of a Z boson has a recoil effect on the emitting top quark. The jets originating from this top quark will therefore tend to have larger momentum than jets from a top quark that did not radiate a Z boson.

Furthermore, explanations for the observation to have more unmatched quarks in $t\bar{t}Z$ events were sought. One reason for this scenario might be a low p_T of the corresponding jet that did not pass the imposed kinematic cuts. A low transverse momentum could also cause the jet not to be among the four highest-p_T jets that are taken by *KLFitter* for the event reconstruction. To validate this assumption, the ratio of the p_T of the fourth and the fifth jets of events containing five or more jets was examined. With a ratio close to 1, the fourth and the fifth jets would have similar transverse momenta. Consequently, the probability would be large for one of the four anticipated final-state jets to be the fifth jet in order of p_T.

A comparison of the ratios for $t\bar{t}Z$ and $t\bar{t}$ is shown in Fig. 5.6b. To highlight the expected effect, the ratio is plotted on a logarithmic scale. The comparison, however, reveals a difference that leads to a contrary effect than expected. With slight deviations between the LO and NLO simulation, the ratio for $t\bar{t}Z$ events is on average significantly higher than that of $t\bar{t}$ events. As a consequence, the average difference between the transverse momenta of the fourth and the fifth jet is higher for $t\bar{t}Z$ events. This observation can be explained with the expected recoil effect that leads to generally higher jet p_T values of the four expected jets. However, as it has a contrary effect, it cannot be quoted as a cause for the observed fraction of unmatched quarks.

5.4. On-Shell and Off-Shell Contributions

To gain further insights into the performance of the dedicated $t\bar{t}Z$ likelihood in *KLFitter*, its parameters were varied. For one reconstruction run, the fraction of on-shell events was set to $f_{\mathrm{on}} = 1$. In this case, the function that is used to fit the invariant mass of the two leptons from the Z boson corresponds to a pure Breit-Wigner distribution. As this modified likelihood only accounts for lepton pairs that are produced via on-shell Z bosons, an overall worse efficiency in the lepton reconstruction is expected. Hereinafter, this modification will be labelled as a dedicated *on-shell likelihood*.

As another modification, events were also reconstructed with the on-shell fraction set to $f_{\mathrm{on}} = 0$ corresponding to a pure $1/m_{ll}^2$ distribution. Also this is presumed to lead to a

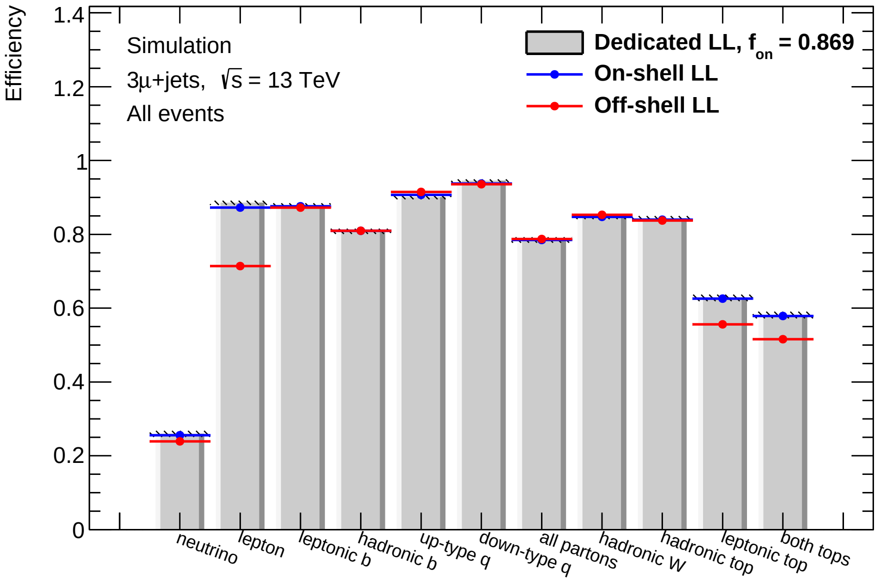

Figure 5.7.: Comparison of a pure on-shell and off-shell likelihood with the dedicated $t\bar{t}Z$ likelihood introduced in Eq. (4.9). The reconstruction efficiencies are determined with the NLO $t\bar{t}Z$ sample. Whereas the on-shell likelihood shows a comparable performance, the off-shell likelihood has significantly lower efficiencies, especially in the reconstruction of the lepton.

lower lepton reconstruction efficiency since this distribution is only valid for lepton pairs that are produced off-shell. As introduced in Section 4.3, the naming convention *off-shell* includes production via γ^*, via γ^*/Z interference as well as via highly virtual Z^* bosons. In what follows, this modification will be called *off-shell likelihood*.

Figure 5.7 shows a comparison between the dedicated on-shell and off-shell likelihoods. As a reference, following the formula in Eq. (4.9), the dedicated $t\bar{t}Z$ likelihood with an on-shell fraction of $f_{\text{on}} = 0.869$ is plotted. As discussed in Section 4.4.2, this value had been determined to be the fraction of on-shell events in the truth record of the NLO simulation. The on-shell likelihood shows an overall similar performance compared to the dedicated likelihood. Reconstruction efficiencies vary within uncertainties, except for the matching of the lepton: even considering uncertainties, its reconstruction is better with the dedicated likelihood. While the on-shell likelihood reconstructs the lepton with 87.3% ± 0.6% efficiency, the dedicated likelihood reaches a value of 88.5% ± 0.6%. On the contrary, the off-shell likelihood performs significantly worse for the lepton. The poor matching also propagates to the neutrino matching and the combined variable of the leptonic top quark.

Additionally, the matching performance of all three likelihoods were also checked for only certain types of events: a cut within the truth record was imposed to only select events that are flagged as *on-shell*. The resulting matching efficiencies are depicted in

Table 5.1.: Comparison of the lepton reconstruction efficiencies for the dedicated, the on-shell and the off-shell likelihood. Following the imposed cuts of Fig. 5.8 and Fig. 5.9, the table also displays the efficiencies when only on-shell events and only off-shell events are processed.

efficiency in %	all events	on-shell events only	off-shell events only
dedicated LL	88.5 ± 0.6	90.5 ± 0.6	69.9 ± 2.4
on-shell LL	87.3 ± 0.6	90.2 ± 0.6	58.4 ± 2.9
off-shell LL	71.4 ± 0.8	70.5 ± 0.9	80.1 ± 2.1

Fig. 5.8. The on-shell and the dedicated likelihood show a very similar performance to that for all events, although the lepton matching efficiencies are slightly increased to 90.2% ± 0.6% and 90.5% ± 0.6%, respectively. Again, the off-shell likelihood performs considerably worse for the lepton and the other variables of the topology of the leptonic top quark, such as the neutrino and the top quark itself.

Figure 5.9 shows another comparison of reconstruction efficiencies for the three likelihoods. For these efficiencies, a truth-record cut was imposed that only filters events labelled as *off-shell*. Within uncertainties, all three likelihoods show a similar performance for all displayed matching efficiencies, except for that of the lepton. With a value of 80.1% ± 2.1%, the off-shell likelihood performs substantially better when compared to the on-shell likelihood, which only reaches an efficiency of 58.4% ± 2.9%. The dedicated $t\bar{t}Z$ likelihood shows an intermediate performance for the lepton. With an efficiency of 69.9% ± 2.4%, it is well above the value of the on-shell likelihood, but does not reach the quality of the performance of the off-shell likelihood.

A complete overview of all lepton matching efficiencies for all types of events and all tested likelihoods can also be found in Table 5.1.

5.5. Possible Separation Power

Using a systematic method to reconstruct the final state also brings different variables that quantify the reconstruction. The simplest variable when using *KLFitter* is its likelihood output. A motivation for the systematic reconstruction method introduced in this thesis was also a possible application of the likelihood output value as a separating variable. If the likelihood values for the $t\bar{t}Z$ reconstruction resulted in a different distribution when applied to a Monte-Carlo simulation of a background process, it could be used as an input variable for multivariate analysis techniques, such as neural networks.

Following that idea, the dedicated likelihood was used to process simulations of diboson samples. These included $4l$, $ll l\nu$ and $ll\nu\nu$ samples leading to a similar final state,

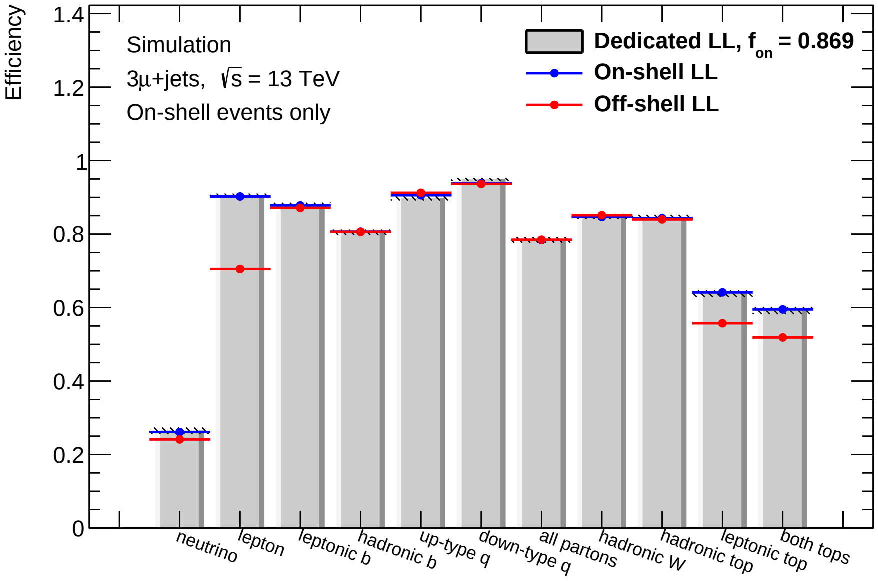

Figure 5.8.: Reconstruction efficiencies of pure on-shell and off-shell likelihoods compared to the dedicated $t\bar{t}Z$ likelihood. As opposed to Fig. 5.7, events are only processed if they are labelled as "on-shell" in the truth record. While the on-shell and dedicated likelihoods have comparable performances, the off-shell likelihood shows significantly worse matching of the lepton.

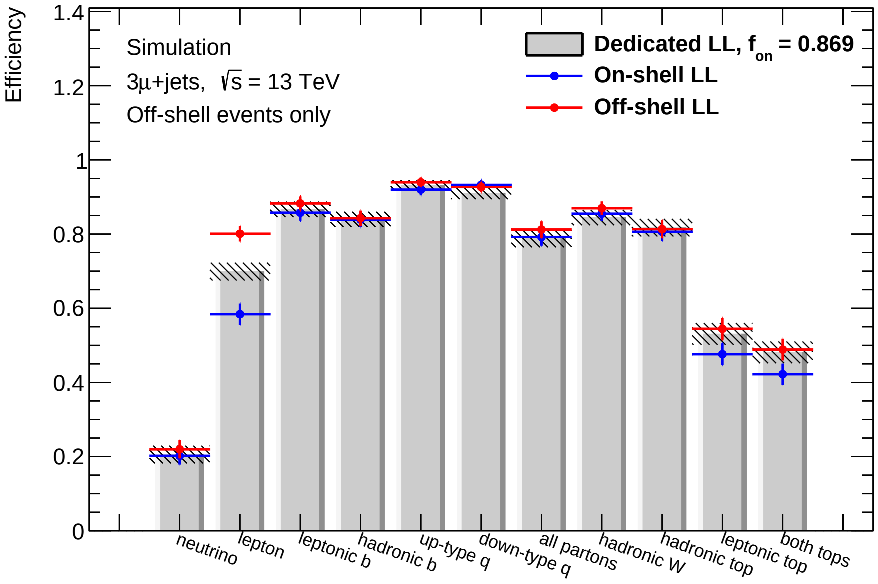

Figure 5.9.: Reconstruction efficiencies of pure on-shell and off-shell likelihoods compared to the dedicated $t\bar{t}Z$ likelihood. As opposed to Fig. 5.7, events are only processed if they are labelled as "off-shell" in the truth record. Whereas the lepton matching of the off-shell likelihood is considerably better than that of the on-shell likelihood, the dedicated likelihood shows an intermediate performance.

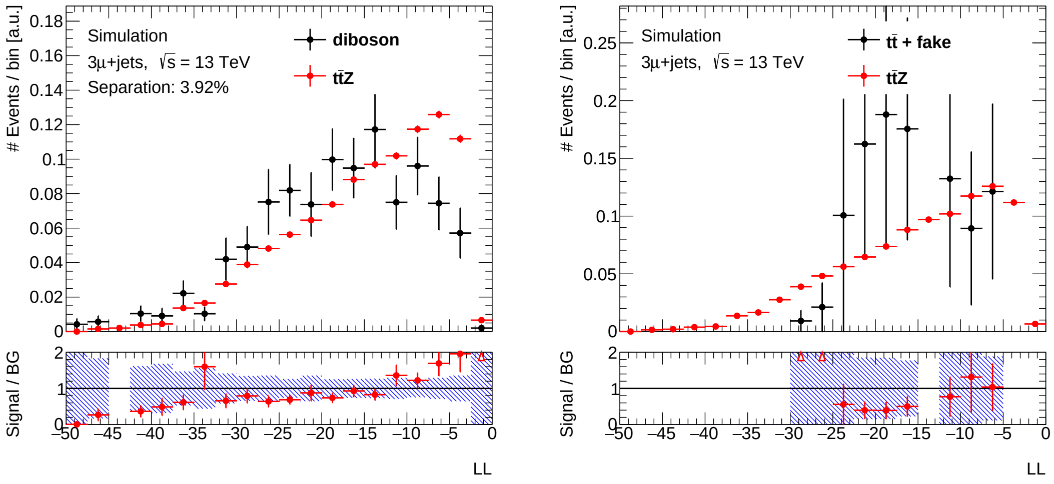

(a) **(b)**

Figure 5.10.: Comparison of the logarithmic likelihood values for $t\bar{t}Z$ and a) diboson and b) $t\bar{t}$+fake events. The three types of events are processed with the dedicated $t\bar{t}Z$ likelihood as introduced in Eq. (4.9) and the *WorkingPoint* jet assignment mode. The plots show distributions of the logarithmic likelihood values of the best permutations. Although limited in statistics, the diboson comparison proves the likelihood value to be a possible separation variable. $t\bar{t}$+fake is too limited in terms of statistics to allow any interpretation.

when additional jets are produced.[4] A comparison of the logarithmic likelihood output (LL) for $t\bar{t}Z$ events and the diboson events is displayed in Fig. 5.10a. Both types of events were processed with the $t\bar{t}Z$ likelihood introduced in Eq. (4.9) and the *WorkingPoint* jet assignment mode. Although limited in terms of statistics of the diboson sample, the plot clearly shows a distinctly different distribution for the two event types. Especially in the region $-10 < LL < 0$, the two distributions deviate notably.

A similar processing was performed for $t\bar{t}$+fake events which is another major background of the trileptonic channel. In this case, the two top quarks are both expected to decay leptonically. An additional third, non-prompt lepton could then result from heavy-flavour decay of one of the jets. This type of process, as it only reaches an identical final state with a non-prompt lepton, is usually called a *fake* background. In Fig. 5.10b, the likelihood output of the reconstruction is compared to that of $t\bar{t}Z$ events. Unfortunately, the number of simulated $t\bar{t}$ events is not high enough for the plot to show any significant results.

---

[4] Strictly speaking, only $ll\nu$ events would have the exact number of leptons and neutrinos that are expected in the trileptonic $t\bar{t}Z$ channel, but in the $4l$ case, one lepton could be missed during detection. Additionally, $ll\nu\nu$ events could have one additional non-prompt lepton from a heavy-flavour decay.

6. Summary & Conclusions

Various experiments have shown the predictions of the Standard Model in the quark sector to be very accurate. The top quark, discovered in 1995, has been under investigation at both the TEVATRON and the LHC colliders for the past twenty years. Nonetheless, some of its properties, such as the weak isospin component I_3, have not been measured directly yet. On the one hand, a precise measurement of I_3 could lead to a confirmation of the Standard Model prediction of $I_3 = +1/2$ and confirm the top quark to be the weak isospin partner of the bottom quark. On the other hand, measurements would open doors to new physics if they established $I_3 \neq +1/2$ and proved the Standard Model to be inaccurate. A direct access to the weak isospin of the top quark is given by $t\bar{t}Z$ processes in which a Z boson is radiated from one of the two top quarks. Measurements of the $t\bar{t}Z$ cross section are one of the key steps to verify the strength and structure of the coupling between the top quark and the Z boson, as introduced in Eq. (2.22). One important quantity to verify the Standard Model predictions would be the fraction of the cross sections of $t\bar{t}Z$ and $t\bar{t}$ events.

For precise measurements of the value of I_3, however, details of the $t\bar{t}Z$ final state, such as angular distributions between individual particles, have to be studied. One problem with the final state of $t\bar{t}Z$ events is its accessibility as all three initial particles decay well before any detection. Within this thesis, kinematic likelihood fits were introduced as a systematic method to assess the resulting, very complex final states of $t\bar{t}Z$ events. The next section briefly summarises the achieved results.

6.1. Performed Studies

Using the *KLFitter* package, studies of the reconstruction efficiency of the trileptonic $t\bar{t}Z$ channel were performed. With three anticipated leptons in the final state, the trileptonic $t\bar{t}Z$ channel comes with many more difficulties than the $t\bar{t}$ lepton+jets channel with only one lepton. Hence, to establish a sophisticated $t\bar{t}Z$ reconstruction, different lepton selection modes were examined. The *Leading* mode uses the established likelihood calculation of the lepton+jets channel in *KLFitter* and therefore assumes the highest-p_T lepton to originate from the leptonically decaying top quark. This method showed poor performance for the lepton reconstruction. The *AmongThree* mode, however, introduced a systematic assignment of the three leptons based on invariant masses of two-lepton systems. The two leptons that had an invariant mass closest to the mass of the Z boson were decided to originate from it, whereas the third lepton was ascribed to the leptonic top quark. With the results presented in Fig. 5.1 it could be proven that this systematic assignment leads to an increase of the lepton reconstruction efficiency of approximately 200%. Significant improvements of the quark matching efficiencies were achieved when using the *WorkingPoint* mode that introduces weighting factors based on b-tagging information.

Furthermore, a dedicated likelihood for $t\bar{t}Z$ events was introduced, as seen in Eq. (4.9). When compared to the lepton+jets likelihood, the added terms include transfer functions for the two additional leptons as well as a term that accounts for the anticipated invariant-mass distribution of these two leptons. The *Dedicated* lepton selection mode that is based on this dedicated likelihood revealed another performance increase in the lepton reconstruction efficiency of approximately 5%.

By examining the truth record of NLO $t\bar{t}Z$ Monte-Carlo simulations, it was found that a significant fraction of 13% of lepton pairs is not produced via on-shell Z bosons, but by what was labelled as the *off-shell* contribution. The observed distribution in Fig. 4.3 approximately follows a $1/m_{ll}^2$ distribution which corresponds to the expectation of lepton pairs produced solely via photons. As a consequence, the invariant-mass distribution within the likelihood was designed in such a way that it accounts both for on-shell and off-shell contributions. A corresponding weighting factor between both components was introduced. It was determined from the fractions of on-shell and off-shell events observed in the truth record when cuts on the lepton kinematics are taken into account.

For a better assessment of the performance, the results were compared to the reconstruction efficiencies achieved in the lepton+jets channel of $t\bar{t}$ events. Although falling short in the lepton reconstruction efficiency, the *KLFitter* performance for $t\bar{t}Z$ events is overall comparable to that for $t\bar{t}$ events. Remarkably, all other matching observables yield higher values in the $t\bar{t}Z$ reconstruction. A comparison of the quark matching revealed a larger portion of events with unmatched quarks. To seek possible explanations, the kinematics of the jets of both processes were compared. Despite slight deviations between LO and NLO simulations of $t\bar{t}Z$ events, they showed significantly different behaviour when compared to $t\bar{t}$ events: the four anticipated jets of $t\bar{t}Z$ events tend to have larger transverse momenta compared to those of $t\bar{t}$ events. Nonetheless, within the jet kinematics studies, no possible explanations for the larger fraction of unmatched quarks could be found.

To verify the necessity of a complex dedicated $t\bar{t}Z$ likelihood that accounts for both on-shell and off-shell contributions, its reconstruction efficiencies were also compared with pure on-shell and off-shell likelihoods. Whereas the former only includes a Breit-Wigner distribution for on-shell events, the latter assumes a $1/m_{ll}^2$ invariant-mass distribution. When processing all events of the Monte-Carlo simulation, the dedicated likelihood showed a significantly better lepton matching than the pure on-shell likelihood. The off-shell likelihood showed an overall poor matching performance for leptons.

Considering only events that are labelled as *on-shell* in the truth record, the performances of the dedicated and on-shell likelihood were similar within uncertainties, whereas the off-shell likelihood again performed considerably worse. When only *off-shell* events are processed, the off-shell likelihood showed by far the best overall performance. With a lepton matching efficiency more than 20% lower, the on-shell likelihood had substantially worse performance. The dedicated likelihood, however, showed an intermediate lepton matching efficiency while its other efficiencies agreed with those of the off-shell likelihood within uncertainties.

As a last step, the *KLFitter* likelihood output was examined for possible separation power between signal and background. For that, the $t\bar{t}Z$ reconstruction was run for diboson and $t\bar{t}$+fake Monte-Carlo simulations, both major backgrounds of the trileptonic $t\bar{t}Z$ channel. Despite the limited statistics of the Monte-Carlo background simulation, the comparison between $t\bar{t}Z$ and diboson events showed a clear separation in the likelihood distribution. It could therefore serve as a separation variable in future analyses in the trileptonic $t\bar{t}Z$ sector and enable separation between signal and background. The comparison between $t\bar{t}$+fake and $t\bar{t}Z$ events, on the contrary, did not allow any interpretation due to the lack of statistics in the $t\bar{t}$+fake simulation.

6.2. Outlook

An accurate reconstruction of the final state is an important prerequisite for precision measurements of the top quark's weak isospin. It was shown that the introduced dedicated likelihood provides significantly higher reconstruction efficiencies than a simple method to assign the lepton pair of the Z boson according to invariant masses. Additionally, the comparison to a pure Breit-Wigner-based likelihood showed a better performance on the side of the dedicated likelihood. Consequently, the introduced likelihood currently provides the best access to the final state of trileptonic $t\bar{t}Z$ events and can be used for future analyses and precision measurements. The achieved reconstruction allows the four momenta of the particles and, as a result, the angles between them to be determined. With enough data collected to enable precision measurements, the reconstruction methods could therefore eventually be used to measure the weak isospin component of the top quark.

Additionally, it was presented that the likelihood output of the *KLFitter* reconstruction comes with separation power to discriminate the $t\bar{t}Z$ signal against background processes. Consequently, within the $t\bar{t}Z$ sector, this variable can be used as an additional separation variable for multivariate analysis techniques, such as neural networks. Future studies should include tests on how strongly the *KLFitter* output is correlated with other potential separation variables. These include low-level observables, such as transverse momenta and energies, but also combined variables, such as invariant masses between two objects.

Other studies should focus on the presence of objects anticipated in the final state.

As there is the chance to miss one or multiple jets within the reconstruction due to the imposed p_T cuts or due to overlap, modifications of the introduced likelihood with only three jet objects have to be examined. This will also cover potential searches in the boosted regime where some of the final-state objects cannot be resolved fully anymore and form strongly-overlapping objects on detector level.

Acknowledgements

First and foremost, I would like to thank Prof. Dr. Arnulf Quadt for giving me the opportunity to work with him and to spend my master's research year in his group. This experience has encouraged me to start a Ph. D. and I am looking forward to continuing our successful cooperation. I would also like to thank Prof. Dr. Stan Lai for being always approachable and for his agreement to be the second referee for this thesis.

The studies and results of this thesis would have been impossible without the daily dialogue with Dr. Boris Lemmer. His ability to always have sympathetic ears for questions and discussions and his creative input were an inspiration and motivation. I am also thankful for the regular feedback and the fruitful discussions with Dr. Lisa Shabalina and Dr. María Moreno Llácer.

One of the driving forces of a successful project is also the quality of the working environment. I would specifically like to thank my office mates Konstantin, Julia and Enrico who all left the institute in the past months. It was a pleasure to work with the three of you and your empty seats will be difficult to fill. I would also like to mention Alexander who joined the institute as a summer intern in my last three months and continued the studies I had started. I hope you enjoyed the time as much as I did! Generally, I would like to thank everyone from Prof. Quadt's working group and the rest of the institute for hosting me in the past twelve months.

My last thanks goes to the three people that proofread all my chapters.

Bibliography

[1] V. C. Rubin, N. Thonnard, and W. K. Ford Jr., *Rotational properties of 21 SC galaxies with a large range of luminosities and radii, from NGC 4605 /R = 4kpc/ to UGC 2885 /R = 122 kpc/*, Astrophys. J. 238 (1980), 471

[2] R. Davis, D. S. Harmer, and K. C. Hoffman, *Search for Neutrinos from the Sun*, Phys. Rev. Lett. 20 (1968), 1205

[3] Y. Fukuda et al.(Super-Kamiokande Collaboration), *Evidence for Oscillation of Atmospheric Neutrinos*, Phys. Rev. Lett. 81 (1998), 1562, arXiv: `hep-ex/9807003`

[4] Q. R. Ahmad et al.(SNO Collaboration), *Measurement of the Rate of* $\nu_e + d \rightarrow p + p + e^-$ *Interactions Produced by* ^8B *Solar Neutrinos at the Sudbury Neutrino Observatory*, Phys. Rev. Lett. 87 (2001), 071301, arXiv: `nucl-ex/0106015`

[5] ATLAS Collaboration, *Observation of a new particle in the search for the Standard Model Higgs boson with the ATLAS detector at the LHC*, Phys. Lett. B 716 (2012), 1, arXiv: `1207.7214`

[6] CMS Collaboration, *Observation of a new boson at a mass of 125 GeV with the CMS experiment at the LHC*, Phys. Lett. B 716 (2012), 30, arXiv: `1207.7235`

[7] P. W. Higgs, *Broken Symmetries, Massless Particles and Gauge Fields*, Phys. Lett. 12 (1964), 132

[8] F. Englert and R. Brout, *Broken Symmetry and the Mass of Gauge Vector Mesons*, Phys. Rev. Lett. 13 (1964), 321

[9] F. Abe et al.(CDF Collaboration), *Observation of Top Quark Production in* $\bar{p}p$ *Collisions with the Collider Detector at Fermilab*, Phys. Rev. Lett. 74 (1995), 2626, arXiv: `hep-ex/9503002`

[10] S. Abachi et al.(DØ Collaboration), *Observation of the Top Quark*, Phys. Rev. Lett. 74 (1995), 2632, arXiv: `hep-ex/9503003`

[11] CMS Collaboration, *Observation of top quark pairs produced in association with a vector boson in pp collisions at* $\sqrt{s} = 8$ *TeV*, JHEP 1601 (2016), 096, arXiv: `1510.01131`

[12] J. Erdmann et al., *A likelihood-based reconstruction algorithm for top-quark pairs and the KLFitter framework*, Nucl. Instrum. Meth. A748 (2014), 18, arXiv: `1312.5595`

[13] S. L. Glashow, *Partial-symmetries of weak interactions*, Nucl. Phys. 22 (1961), 579

[14] S. Weinberg, *A Model of Leptons*, Phys. Rev. Lett. 19 (1967), 1264

[15] A. Salam, *Weak and Electromagnetic Interactions*, *Elementary particle theory, Relativistic groups and analyticity*, Proceedings of the Eighth Nobel Symposium, (May 19–25, 1968), Stockholm: Almquist & Wiksell, 1968, 367

[16] S. L. Glashow, J. Iliopoulos, and L. Maiani, *Weak Interactions with Lepton-Hadron Symmetry*, Phys. Rev. D 2 (1970), 1285

[17] H. Georgi and S. L. Glashow, *Unified weak and electromagnetic interactions without neutral currents*, Phys. Rev. Lett. 28 (1972), 1494

[18] H. D. Politzer, *Reliable Perturbative Results for Strong Interactions?*, Phys. Rev. Lett. 30 (1973), 1346

[19] H. D. Politzer, *Asymptotic Freedom: An Approach to Strong Interactions*, Phys. Rept. 14 (1974), 129

[20] D. J. Gross and F. Wilczek, *Ultraviolet Behavior of Nonabelian Gauge Theories*, Phys. Rev. Lett. 30 (1973), 1343

[21] G. 't Hooft, *Renormalizable Lagrangians for Massive Yang-Mills Fields*, Nucl. Phys. B 35 (1971), 167

[22] G. 't Hooft and M. Veltman, *Regularization and renormalization of gauge fields*, Nucl. Phys. B 44 (1972), 189

[23] G. 't Hooft and M. Veltman, *Combinatorics of gauge fields*, Nucl. Phys. B 50 (1972), 318

[24] K. A. Olive et al.(Particle Data Group), *Review of Particle Physics*, Chin. Phys. C38 (2014), 090001

[25] D. J. Gross and F. Wilczek, *Asymptotically Free Gauge Theories. 1*, Phys. Rev. D 8 (1973), 3633

[26] C. S. Wu et al., *Experimental Test of Parity Conservation in Beta Decay*, Phys. Rev. 105 (1957), 1413

[27] N. Cabibbo, *Unitary Symmetry and Leptonic Decays*, Phys. Rev. Lett. 10 (1963), 531

[28] M. Kobayashi and T. Maskawa, *CP Violation in the Renormalizable Theory of Weak Interaction*, Prog. Theor. Phys. 49 (1973), 652

[29] J. W. Cronin et al., *Evidence for the* 2π *Decay of the* K_2^0 *Meson*, Phys. Rev. Lett. 13 (1964), 138

[30] M. L. Perl et al., *Evidence for Anomalous Lepton Production in* $e^+ - e^-$ *Annihilation*, Phys. Rev. Lett. 35 (1975), 1489

[31] S. W. Herb et al., *Observation of a Dimuon Resonance at 9.5 GeV in 400-GeV Proton-Nucleus Collisions*, Phys. Rev. Lett. 39 (1977), 252

[32] M. Gell-Mann, *The interpretation of the new particles as displaced charge multiplets*, Nuovo Cim. 4 (1956), 848

[33] T. Nakano and K. Nishijima, *Charge Independence for V-particles*, Prog. Theor. Phys. 10 (1953), 581

[34] H. Georgi and S. L. Glashow, *Making Do Without the T Quark*, Nucl. Phys. B 167 (1980), 173

[35] G. L. Kane and M. E. Peskin, *A Constraint from B Decay on Models with No T Quark*, Nucl. Phys. B 195 (1982), 29

[36] H. Georgi and A. Pais, *Generalization of Gim: Horizontal and Vertical Flavor Mixing*, Phys. Rev. D 19 (1979), 2746

[37] F. Gursey, P. Ramond, and P. Sikivie, *A Universal Gauge Theory Model Based on E6*, Phys. Lett. B 60 (1976), 177

[38] A. Bean et al., *Improved upper limit on flavor-changing neutral-current decays of the b quark*, Phys. Rev. D 35 (1987), 3533

[39] LEP Collaborations, *Electroweak parameters of the* Z^0 *resonance and the standard model*, Phys. Lett. B 276 (1992), 247

[40] Tevatron Electroweak Working Group, *Combination of CDF and D0 results on the mass of the top quark using up* $9.7\,fb^{-1}$ *at the Tevatron*, 2016, arXiv: `1608.01881`

[41] M. Jeżabek and J. H. Kühn, *QCD corrections to semileptonic decays of heavy quarks*, Nucl. Phys. B 314 (1989), 1

[42] I. Bigi et al., *Production and decay properties of ultra-heavy quarks*, Phys. Lett. B 181 (1986), 157

[43] R. D. Ball et al., *Parton distributions with LHC data*, Nucl. Phys. B 867 (2013), 244, arXiv: `1207.1303`

[44] The Durham HepData Project, *Online PDF plotting and calculation*, URL: `http://hepdata.cedar.ac.uk/pdf/pdf3.html` (visited on 03/15/2016)

[45] J. C. Collins, D. E. Soper, and G. F. Sterman, *Heavy Particle Production in High-Energy Hadron Collisions*, Nucl. Phys. B 263 (1986), 37

[46] U. Langenfeld, S. Moch, and P. Uwer, *New results for t anti-t production at hadron colliders, Proceedings, 17th International Workshop on Deep-Inelastic Scattering and Related Subjects (DIS 2009)*, 2009, arXiv: `0907.2527`

[47] M. Czakon and A. Mitov, *Top++: A Program for the Calculation of the Top-Pair Cross-Section at Hadron Colliders*, Comput. Phys. Commun. 185 (2014), 2930, arXiv: `1112.5675`

[48] M. Botje et al., *The PDF4LHC Working Group Interim Recommendations*, 2011, arXiv: 1101.0538

[49] A. D. Martin et al., *Uncertainties on alpha(S) in global PDF analyses and implications for predicted hadronic cross sections*, Eur. Phys. J. C64 (2009), 653, arXiv: 0905.3531

[50] J. Gao et al., *CT10 next-to-next-to-leading order global analysis of QCD*, Phys. Rev. D 89 (2014), 033009, arXiv: 1302.6246

[51] ATLAS Collaboration, *Measurement of the $t\bar{t}$ production cross-section using $e\mu$ events with b-tagged jets in pp collisions at $\sqrt{s}$=13 TeV with the ATLAS detector*, Phys. Lett. B761 (2016), 136, arXiv: 1606.02699

[52] LHC Top Physics Working Group, *LHCTopWG Summary Plots*, URL: https://twiki.cern.ch/twiki/bin/view/LHCPhysics/LHCTopWGSummaryPlots (visited on 08/14/2016)

[53] V. M. Abazov et al.(DØ Collaboration), *Observation of Single Top-Quark Production*, Phys. Rev. Lett. 103 (2009), 092001, arXiv: 0903.0850

[54] T. Aaltonen et al.(CDF Collaboration), *Observation of Electroweak Single Top-Quark Production*, Phys. Rev. Lett. 103 (2009), 092002, arXiv: 0903.0885

[55] J. M. Campbell et al., *A Monte Carlo for FeMtobarn processes at Hadron Colliders*, URL: http://mcfm.fnal.gov (visited on 03/18/2016)

[56] S. Schael et al.(SLD Electroweak Group, DELPHI, ALEPH, SLD, SLD Heavy Flavour Group, OPAL, LEP Electroweak Working Group, L3), *Precision electroweak measurements on the Z resonance*, Phys. Rept. 427 (2006), 257

[57] J. Alwall et al., *The automated computation of tree-level and next-to-leading order differential cross sections, and their matching to parton shower simulations*, JHEP 1407 (2014), 079, arXiv: 1405.0301

[58] ATLAS Collaboration, *Search for $t\bar{t}Z$ production in the three lepton final state with 4.7 fb^{-1} of $\sqrt{s}$ = 7 TeV pp collision data collected by the ATLAS detector*, ATLAS-CONF-2012-126, 2012

[59] CMS Collaboration, *Measurement of associated production of vector bosons and top quark-antiquark pairs at sqrt(s) = 7 TeV*, Phys. Rev. Lett. 110 (2013), 172002, arXiv: 1303.3239

[60] ATLAS Collaboration, *Measurement of the $t\bar{t}W$ and $t\bar{t}Z$ production cross sections in pp collisions at $\sqrt{s}$ = 8 TeV with the ATLAS detector*, JHEP 1511 (2015), 172, arXiv: 1509.05276

[61] ATLAS Collaboration, *Measurement of the $t\bar{t}Z$ and $t\bar{t}W$ production cross sections in multilepton final states using 3.2 fb^{-1} of pp collisions at $\sqrt{s} = 13$ TeV with the ATLAS detector*, Submitted to Eur. Phys. J. C, 2016, arXiv: 1609.01599

[62] CMS Collaboration, *Measurement of the top pair-production in association with a W or Z boson in pp collisions at 13 TeV*, CMS-PAS-TOP-16-017, 2016

[63] ATLAS Collaboration, *Luminosity Public Results*, URL: https://twiki.cern.ch/twiki/bin/view/AtlasPublic/LuminosityPublicResults (visited on 09/25/2016)

[64] ATLAS Collaboration, *ATLAS Detector and Physics Performance TDR, Volume I+II*, CERN/LHCC 99-14/15, 1999

[65] ATLAS Collaboration, *ATLAS high-level trigger, data-acquisition and controls: Technical Design Report*, CERN-LHCC-2003-022, 2003

[66] ATLAS Collaboration, *ATLAS level-1 trigger: Technical Design Report*, CERN-LHCC-98-014, 1998

[67] W. Panduro Vazquez(on behalf of the ATLAS Collaboration), *The ATLAS Data Acquisition System: from Run 1 to Run 2*, Nucl. Part. Phys. Proc. 273-275 (2016), 939

[68] ATLAS Collaboration, *Electron reconstruction and identification efficiency measurements with the ATLAS detector using the 2011 LHC proton-proton collision data*, Eur. Phys. J. C74 (2014), 2941

[69] ATLAS Collaboration, *Expected electron performance in the ATLAS experiment*, ATL-PHYS-PUB-2011-006, 2011

[70] ATLAS Collaboration, *Electron efficiency measurements with the ATLAS detector using the 2012 LHC proton-proton collision data*, ATLAS-CONF-2014-032, 2014

[71] ATLAS Collaboration, *Electron identification measurements in ATLAS using $\sqrt{s} =$ 13 TeV data with 50 ns bunch spacing*, ATL-PHYS-PUB-2015-041, 2015

[72] ATLAS Collaboration, *Muon reconstruction performance in early $\sqrt{s} = 13$ TeV data*, ATL-PHYS-PUB-2015-037, 2015

[73] M. Cacciari, G. P. Salam, and G. Soyez, *The Anti-k(t) jet clustering algorithm*, JHEP 0804 (2008), 063, arXiv: 0802.1189

[74] ATLAS Collaboration, *Performance of b-Jet Identification in the ATLAS Experiment*, JINST 11 (2016), P04008

[75] ATLAS Collaboration, *Performance of Missing Transverse Momentum Reconstruction in Proton-Proton Collisions at 7 TeV with ATLAS*, Eur. Phys. J. C72 (2012), 1844

[76] A. Caldwell, D. Kollar, and K. Kröninger, *BAT: The Bayesian Analysis Toolkit*, Comput. Phys. Commun. 180 (2009), 2197, arXiv: 0808.2552

[77] ATLAS Collaboration, *Measurement of the top quark pair production charge asymmetry in proton-proton collisions at* $\sqrt{s} = 7$ *TeV using the ATLAS detector*, JHEP 1402 (2014), 107, arXiv: `1311.6724`

[78] ATLAS Collaboration, *Measurement of Top Quark Polarization in Top-Antitop Events from Proton-Proton Collisions at* $\sqrt{s} = 7$ *TeV Using the ATLAS Detector*, Phys. Rev. Lett. 111 (2013), 232002, arXiv: `1307.6511`

[79] ATLAS Collaboration, *Measurement of the W boson polarization in top quark decays with the ATLAS detector*, JHEP 1206 (2012), 088, arXiv: `1205.2484`

[80] ATLAS Collaboration, *Measurement of the top quark mass with the template method in the* $t\bar{t} \to \text{lepton}+\text{jets}$ *channel using ATLAS data*, Eur. Phys. J. C72 (2012), 1, arXiv: `1203.5755`

[81] ATLAS Collaboration, *Measurements of top quark pair relative differential cross-sections with ATLAS in* pp *collisions at* $\sqrt{s} = 7$ *TeV*, Eur. Phys. J. C73 (2013), 2261, arXiv: `1207.5644`

[82] ATLAS Collaboration, *Search for the Standard Model Higgs boson produced in association with top quarks in proton-proton collisions at* $\sqrt{s} = 7$ *TeV using the ATLAS detector*, ATLAS-CONF-2012-135, 2012

[83] D. J. Lange, *The EvtGen particle decay simulation package*, Nucl. Instrum. Meth. A462 (2001), 152

[84] ATLAS Collaboration, *The ATLAS Simulation Infrastructure*, Eur. Phys. J. C70 (2010), 823

[85] S. Agostinelli et al., *Geant4—a simulation toolkit*, Nucl. Instrum. Meth. A506 (2003), 250

[86] T. Sjöstrand et al., *An Introduction to PYTHIA 8.2*, Comput. Phys. Commun. 191 (2015), 159, arXiv: `1410.3012`

[87] ATLAS Collaboration, *ATLAS Run 1 Pythia8 tunes*, ATL-PHYS-PUB-2014-021, 2014

[88] ATLAS Collaboration, *Modelling of the* $t\bar{t}H$ *and* $t\bar{t}V$ $(V = W, Z)$ *processes for* $\sqrt{s} = 13$ *TeV ATLAS analyses*, ATL-PHYS-PUB-2016-005, 2016

[89] T. Gleisberg et al., *Event generation with SHERPA 1.1*, JHEP 0902 (2009), 007

[90] P. Nason, *A New method for combining NLO QCD with shower Monte Carlo algorithms*, JHEP 0411 (2004), 040, arXiv: `hep-ph/0409146`

[91] S. Frixione, P. Nason, and C. Oleari, *Matching NLO QCD computations with Parton Shower simulations: the POWHEG method*, JHEP 0711 (2007), 070, arXiv: `0709.2092`

[92] S. Alioli et al., *A general framework for implementing NLO calculations in shower Monte Carlo programs: the POWHEG BOX*, JHEP 1006 (2010), 043, arXiv: `1002.2581`

[93] H.-L. Lai et al., *New parton distributions for collider physics*, Phys. Rev. D 82 (2010), 074024, arXiv: `1007.2241`

[94] T. Sjostrand, S. Mrenna, and P. Z. Skands, *PYTHIA 6.4 Physics and Manual*, JHEP 05 (2006), 026, arXiv: `hep-ph/0603175`

[95] J. Pumplin et al., *New generation of parton distributions with uncertainties from global QCD analysis*, JHEP 07 (2002), 012, arXiv: `hep-ph/0201195`

[96] P. Z. Skands, *Tuning Monte Carlo generators: The Perugia tunes*, Phys. Rev. D 82 (2010), 074018

A. Figures and Tables

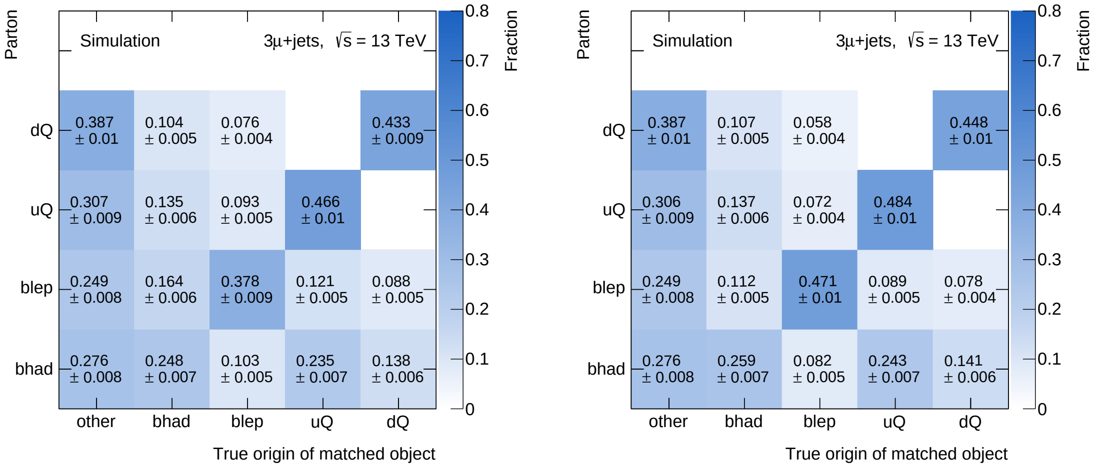

(a) **(b)**

Figure A.1.: Jet matching matrices for NLO $t\bar{t}Z$ events using a) the *Leading* and b) the *AmongThree* lepton selection mode. Both matrices are produced with the *NoTag* jet assignment mode described in Section 4.3. The *AmongThree* mode shows a significant efficiency increase for the matching of b_{lep}.

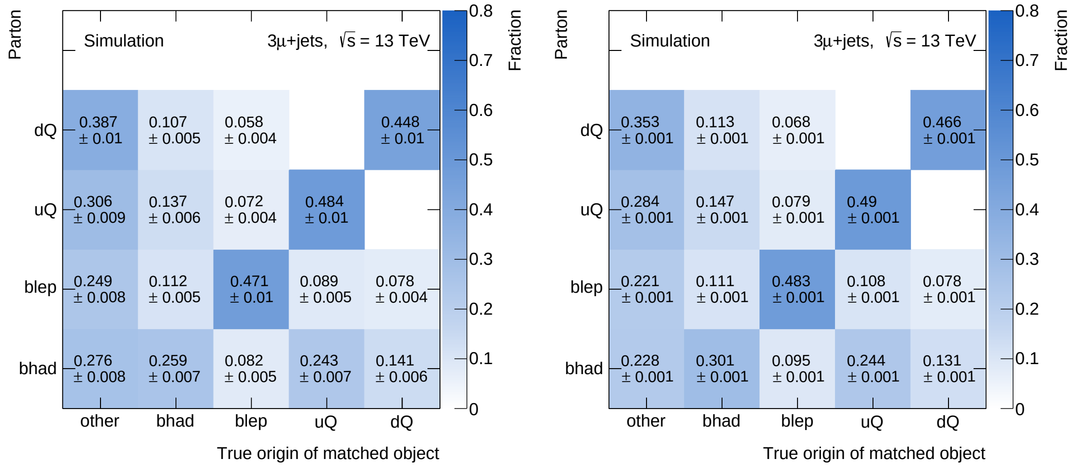

(a) (b)

Figure A.2.: Jet matching matrices for the *NoTag* jet assignment mode introduced in Section 4.3. The matrices show the matching for a) $t\bar{t}Z$ events with the *AmongThree* lepton mode and b) $t\bar{t}$ events, both simulated at NLO. The results are similar to those obtained for matrices of the *WorkingPoint* assignment mode, displayed in Fig. 5.4: the $t\bar{t}$ reconstruction shows higher efficiencies.

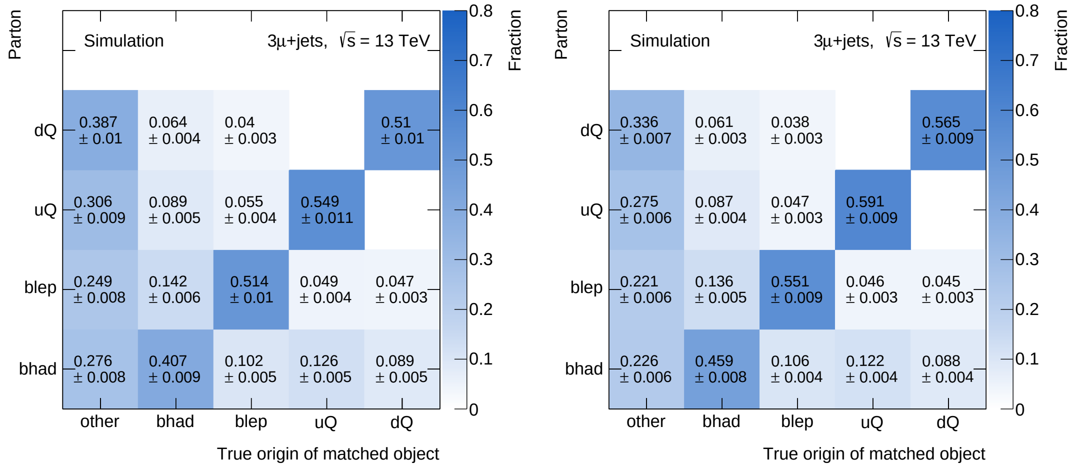

(a) (b)

Figure A.3.: Jet matching matrices the dedicated $t\bar{t}Z$ likelihood. The plots show the matching efficiencies for simulations at a) leading order and b) next-to-leading order.

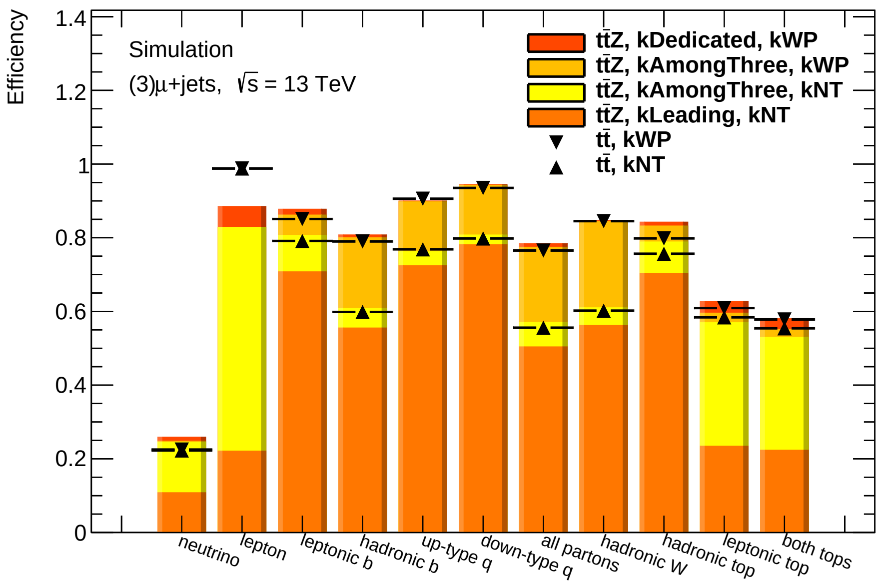

Figure A.4.: Matching efficiencies for $t\bar{t}Z$ and $t\bar{t}$ processes. The diagram shows different lepton selection modes paired with the *NoTag* or the *WorkingPoint* jet assignment modes. Statistical uncertainties of the efficiencies for $t\bar{t}Z$ processes are below 1%, for $t\bar{t}$ processes below 0.1%. They are not displayed to maintain clarity of the plot.

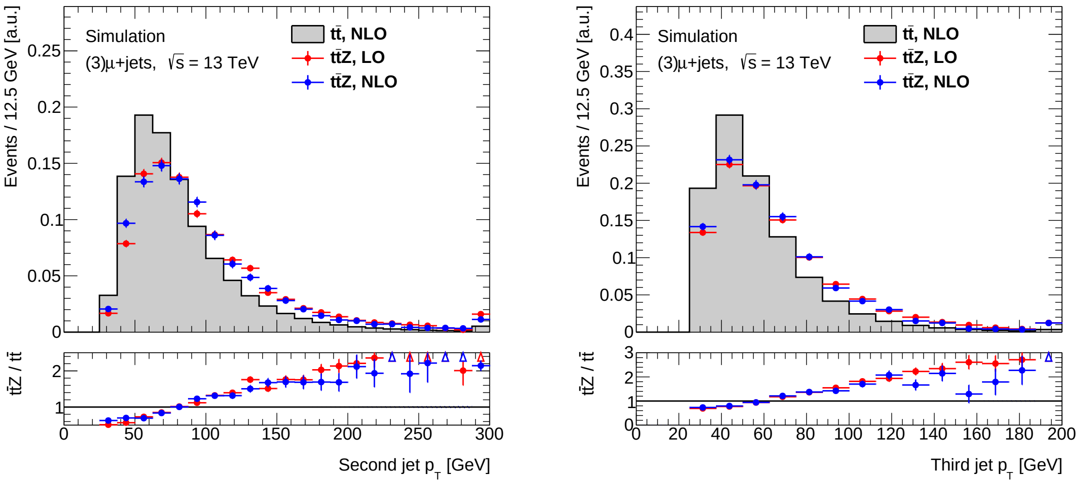

(a) **(b)**

Figure A.5.: Comparison of jet kinematics of $t\bar{t}Z$ and $t\bar{t}$ processes. The plots show the p_T of a) the second jet and b) the third jet.

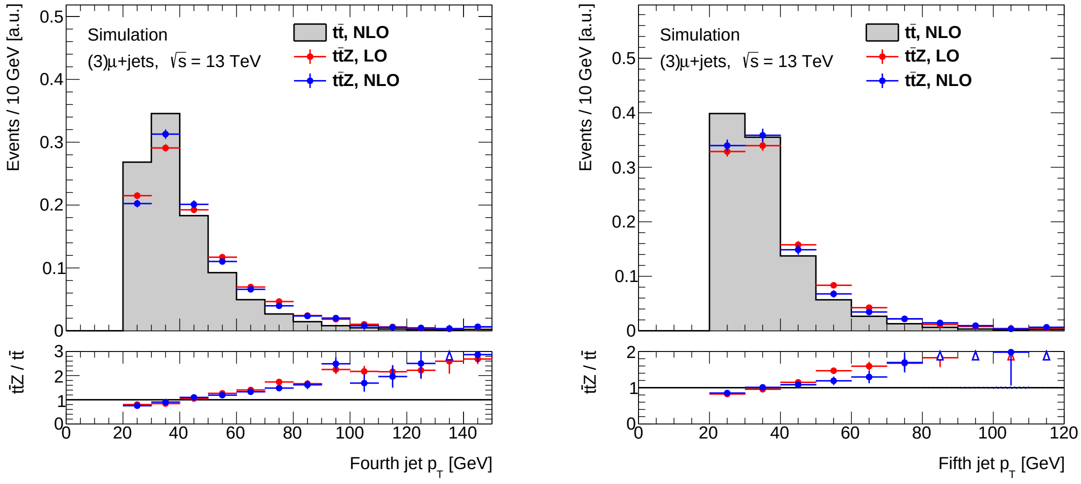

(a) **(b)**

Figure A.6.: Comparison of jet kinematics of $t\bar{t}Z$ and $t\bar{t}$ processes. The plots show the p_T of a) the fourth jet and b) the fifth jet (if existing).

Erklärung nach §17(9) der Prüfungsordnung für den Bachelor-Studiengang Physik und den Master-Studiengang Physik an der Universität Göttingen:

Hiermit erkläre ich, dass ich diese Abschlussarbeit selbständig verfasst habe, keine anderen als die angegebenen Quellen und Hilfsmittel benutzt habe und alle Stellen, die wörtlich oder sinngemäß aus veröffentlichten Schriften entnommen wurden, als solche kenntlich gemacht habe.
Darüberhinaus erkläre ich, dass diese Abschlussarbeit nicht, auch nicht auszugsweise, im Rahmen einer nichtbestandenen Prüfung an dieser oder einer anderen Hochschule eingereicht wurde.

Göttingen, den 30. September 2016

(Knut Zoch)